

ISSN: 2349-6495(P) | 2456-1908 (O)



# International Journal of Advanced Engineering Research and Science

(IJAERS)

An Open Access Peer-Reviewed International Journal



Journal DOI: 10.22161/ijaers

Issue DOI: 10.22161/ijaers.118

AI PUBLICATIONS

Vol.- 11 | Issue - 8 | Aug 2024

editor.ijaers@gmail.com | editor@ijaers.com | <https://www.ijaers.com/>

# International Journal of Advanced Engineering Research and Science (IJAERS)

(ISSN: 2349-6495(P)| 2456-1908(O))

DOI: 10.22161/ijaers

Vol-11, Issue-8

August, 2024

*Editor in Chief*

Dr. Swapnesh Taterh

*Chief Executive Editor*

S. Suman Rajest

---

Copyright © 2024 International Journal of Advanced Engineering Research and Science

Publisher

*AI Publication*

Email: [editor.ijaers@gmail.com](mailto:editor.ijaers@gmail.com); [editor@ijaers.com](mailto:editor@ijaers.com)

Web: [www.ijaers.com](http://www.ijaers.com)

## **International Editorial/ Reviewer Board**

### **Editor in Chief**

- **Dr. Swapnesh Taterh (Chief-Editor)**, Amity University, Jaipur, India

### **Chief Executive Editor**

- **S. Suman Rajest**, Vels Institute of Science, Technology & Advanced Studies, India  
chief-executive-editor@ijaers.com

### **Associate Editors**

- **Dr. Ram Karan Singh**, King Khalid University, Guraiger, Abha 62529, Saudi Arabia
- **Dr. Shuai Li**, University of Cambridge, England, Great Britain

### **Editorial Member**

- **Behrouz Takabi**, PhD, Texas A&M University, Texas, USA
- **Dr. Gamal Abd El-Nasser Ahmed Mohamed Said**, Port Training Institute (PTI), Arab Academy For Science, Technology and Maritime Transport, Egypt
- **Dr. Hou, Cheng-I**, Chung Hua University, Hsinchu Taiwan
- **Dr. Ebrahim Nohani**, Islamic Azad University, Dezful, IRAN.
- **Dr. Ahmadad Nabih Zaki Rashed**, Menoufia University, EGYPT
- **Dr. Rabindra Kayastha**, Kathmandu University, Nepal
- **Dr. Dinh Tran Ngoc Huy**, Banking and Finance, HCM, Viet Nam
- **Dr. Engin NAS**, Duzce University, Turkey
- **Dr. A. Heidari**, California South University (CSU), Irvine, California, USA
- **Dr. Uma Choudhary**, Mody University, Lakshmangarh, India
- **Dr. Varun Gupta**, National Informatic Center, Delhi, India
- **Dr. Ahmed Kadhim Hussein**, University of Babylon, Republic of Iraq
- **Dr. Vibhash Yadav**, Rajkiya Engineering College, Banda. UP, India
- **Dr. M. Kannan**, SCSVMV University, Kanchipuram, Tamil Nadu, India
- **José G. Vargas-Hernández**, University of Guadalajara Periférico Norte 799 Edif. G201-7, Núcleo Universitario Los Belenes, Zapopan, Jalisco, 45100, México
- **Dr. Sambit Kumar Mishra**, Gandhi Institute for Education and Technology, Baniatangi, Bhubaneswar, India
- **DR. C. M. Velu**, Datta Kala Group of Institutions, Pune, India
- **Dr. Deependra Pandey**, Amity University, Uttar Pradesh, India
- **Dr. K Ashok Reddy**, MLR Institute of Technology, Dundigal, Hyderabad, India
- **Dr. S.R.Boselin Prabhu**, SVS College of Engineering, Coimbatore, India
- **N. Balakumar**, Tamilnadu College of Engineering, Karumathampatti, Coimbatore, India
- **R. Poorvadevi**, SCSVMV University, Enathur, Kanchipuram, Tamil Nadu, India
- **Dr. Subha Ganguly**, Arawali Veterinary College, Sikar, India
- **Dr. P. Murali Krishna Prasad**, GVP College of Engineering for Women, Visakhapatnam, Andhra Pradesh, India
- **Anshul Singhal**, Bio Instrumentation Lab, MIT, USA
- **Mr. Lusekelo Kibona**, Ruaha Catholic University, Iringa, Tanzania
- **Sina Mahdavi**, Urmia Graduate Institute, Urmia, Iran
- **Dr. N. S. Mohan**, Manipal Institute of Technology, Manipal, India
- **Dr. Zafer Omer Ozdemir**, University of Health Sciences, Haydarpassa, Uskudar, Istanbul, TURKIYE
- **Bingxu Wang**, 2721 Patrick Henry St Apt 510, Auburn Hills, Michigan, United States

- **Dr. Jayashree Patil-Dake**, KPB Hinduja College of Commerce, Mumbai, India
- **Dr. Neel Kamal Purohit**, S.S. Jain Subodh P.G. College, Rambagh, Jaipur, India
- **Mohd Muntjir**, Taif University, Kingdom of Saudi Arabia
- **Xian Ming Meng**, China Automotive Technology & Research Center No.68, East Xianfeng Road, Dongli District, Tianjin, China
- **Herlandi de Souza Andrade**, FATEC Guaratingueta, State Center for Technological Education Paula Souza - CEETEPS
- **Dr. Payal Chadha**, University of Maryland University College Europe, Kuwait
- **Ahmed Moustafa Abd El-hamid Elmahalawy**, Menoufia University, Al Minufya, Egypt
- **Prof. Mark H. Rummeli**, University & Head of the characterisation center, Soochow Institute for Energy Materials Innovations (SIEMES), Suzhou, Jiangsu Province, China
- **Dr. Eman Yaser Daraghmi**, Ptuk, Tulkarm, Palestine
- **Holmes Rajagukguk**, State University of Medan, Lecturer in Sisingamangaraja University North Tapanuli, Indonesia
- **Dr. Menderes KAM**, Dr. Engin PAK Cumayeri Vocational School, DÜZCE UNIVERSITY (University in Turkey), Turkey
- **Dr. Jatin Goyal**, Punjabi University, Patiala, Punjab, India | International Collaborator of GEITEC / UNIR / CNPq, Brazil
- **Ahmet İPEKÇİ**, Dr. Engin PAK Cumayeri Vocational School, DÜZCE UNIVERSITY, Turkey
- **Baarimah Abdullah Omar**, Universiti Malaysia Pahang (UMP), Gambang, 26300, Malaysia
- **Sabri UZUNER**, Dr. Engin PAK Cumayeri Vocational School Cumayeri/Duzce/Turkey
- **Ümit AĞBULUT**, Düzce University, Turkey
- **Dr. Mustafa ÖZKAN**, Trakya University, Edirne/ TURKEY
- **Dr. Indrani Bhattacharyya**, Dr. B.C. Roy College of Pharmacy and Allied Health Sciences, Durgapur, West Bengal, India
- **Egnon Kouakouc**, Nutrition/Health at University Felix Houphouet Boigny Abidjan, Ivory Coast
- **Dr. Suat SARIDEMİR**, Düzce University, Faculty of Technology, Turkey
- **Dr. Manvinder Singh Pahwa**, Director, Alumni Relations at Manipal University Jaipur, India
- **Omid Habibzadeh Bigdarvish**, University of Texas at Arlington, Texas, USA
- **Professor Dr. Ho Soon Min**, INTI International University, Jln BBN 12/1, Bandar, Baru Nilai, 71800 Negeri Sembilan, Malaysia
- **Ahmed Mohammed Morsy Hassan**, South Egypt Cancer Institute, Assiut University, Assiut, Egypt
- **Xian Ming Meng (Ph.D)**, China Automotive Technology & Research Center, No.68, East Xianfeng Road, Tianjin, China
- **Ömer Erkan**, Konuralp Campus, Düzce-Turkey
- **Dr. Yousef Daradkeh**, Prince Sattam bin Abdulaziz University) PSAU), KSA
- **Peter JO**, IPB University, Indonesia
- **Nazmi Liana Binti Azmi**, Raja Perempuan Zainab II Hospital, 15586 Kota Bharu, Kelantan, Malaysia
- **Mr. Sagar Jamle**, Oriental University, Indore, India
- **Professor Grazione de Souza**, Applied Mathematics, Rio de Janeiro State University, Brazil
- **Kim Edward S. Santos**, Nueva Ecija University of Science and Technology, Philippines.

**Vol-11, Issue-8, August 2024**  
**(10.22161/ijaers.118)**

<b>Detail with DOI (CrossRef)</b>	
<b>A Partially Coupled Turbo Code Design for Error Detection and Correction in IoT Networks</b> Raman Singh Ahirwal, Amit Marmat  DOI: <a href="https://doi.org/10.22161/ijaers.118.1">10.22161/ijaers.118.1</a>	Page No: 01-07
<b>Fire detection algorithm based on the fusion of YOLOv8 and Deformable Conv DCN</b> Lin Po Shang, Yan Zuo Chang, Yi Chen, Yong Shan Ou  DOI: <a href="https://doi.org/10.22161/ijaers.118.2">10.22161/ijaers.118.2</a>	Page No: 08-15
<b>Change in torsion and strength of wires</b> Prakash Gawali, Amit Kumar Kundu  DOI: <a href="https://doi.org/10.22161/ijaers.118.3">10.22161/ijaers.118.3</a>	Page No: 16-18
<b>Development of Intelligent Self-propelled Sprinkler Car Based on Single Chip Computer</b> Jian-Ting Lai, Yan-Zuo Chang, Ruo-Yu Yang, Jin-Ping Chen, Man-Lin Zheng  DOI: <a href="https://doi.org/10.22161/ijaers.118.4">10.22161/ijaers.118.4</a>	Page No: 19-27
<b>Air Conditioning Design for Comfort Impact on the Human Body in Small Vehicles</b> Jin-Ping Chen, Yan-Zuo Chang, Ruo-Yu Yang, Jian-Ting Lai, Pei-Xin Wu  DOI: <a href="https://doi.org/10.22161/ijaers.118.5">10.22161/ijaers.118.5</a>	Page No: 28-35
<b>Research on Noise Mode Prediction of Air Conditioner Based on Training Neural Network Method</b> Ruo-Yu Yang, Yan-Zuo Chang, Jin-Ping Chen, Jian-Ting Lai, Ren-Jia Qin  DOI: <a href="https://doi.org/10.22161/ijaers.118.6">10.22161/ijaers.118.6</a>	Page No: 36-42

# A Partially Coupled Turbo Code Design for Error Detection and Correction in IoT Networks

Raman Singh Ahirwal<sup>1</sup>, Amit Marmat<sup>2</sup>

<sup>1</sup>P.G. Student, Department of Electronic and Telecommunication Engineering, Vikram University/School of Engineering & Technology, Ujjain, M.P., India

Email: raman.singh563@gmail.com

<sup>2</sup> Professor, Department of Electronic and Telecommunication Engineering, Vikram University/School of Engineering & Technology, Ujjain, M.P., India

Email : raman.singh563@gmail.com

Received: 27 Jun 2024,

Receive in revised form: 25 Jul 2024,

Accepted: 02 Aug 2024,

Available online: 07 Aug 2024

©2024 The Author(s). Published by AI  
Publication. This is an open access article under  
the CC BY license

[\(https://creativecommons.org/licenses/by/4.0/\)](https://creativecommons.org/licenses/by/4.0/)

**Keywords—** Internet of things, Turbo Codes,  
trustworthiness, error rate, bit sharing.

**Abstract—** The internet of things framework has seen a rapid change in terms of the applications and users worldwide. However, the need for trustworthiness to satisfactory quality of service is of utmost importance keeping in mind the nature of data transfer in wireless media. The advent of high compute power processors with miniature sizes and low power consumption, implementing relatively complex algorithms has become possible which is necessity for internet of things applications. This research paper focusses on the design and implementation of the code blocks of turbo codes based on the BCJR algorithm so as to couple the bits in the code blocks in the composite transport block. The information and parity bits are to be coupled so as to have more information sharing within the transport block and hence reduce the error rate steeply in section of the error waterfall. The proposed technique attains lower bit error rate performance compared to the conventional un-coded and hard coded counterparts. A comparative analysis with respect to the error rate has been done so as to evaluate the quality of service of the proposed work. The lower error rate of the proposed work ensures the high quality of service and trustworthiness of the IoT system.

## I. INTRODUCTION

One of the major challenges of the internet of things framework is the chances of bit flips in the data to be sent. A typical IoT framework is depicted in figure 1. The IoT framework owing to the wireless or unguided media has to be designed such that it exhibits satisfactory quality of service [1].

The metrics may be considered to be:

- 1) Error Rate
- 2) Throughput
- 3) Latency

Most of the parameters though could be managed under at least one governing constraint which is [2]:



Fig.1 The IoT framework

$$Data\ Rate_c \leq Capacity_c \tag{1}$$

Here,

$Data\ Rate_c$  is the actual data rate through the channel.

$Capacity_c$  denotes the permissible channel capacity of the IoT network.

The IoT framework typically exhibits a steep fall in the waterfall region of the error curve and then a diminishing error rate [3].

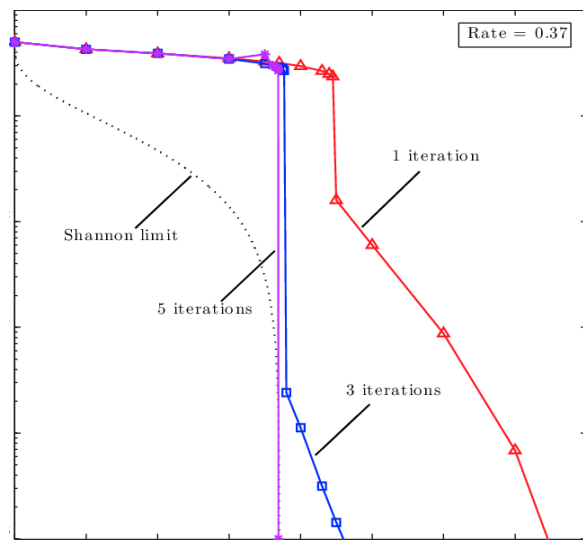


Fig.2 Typical error performance of Shannon's limit

The typical Shannon's limit is exhibited by a sharp fall in the bit error rate upto or beyond  $10^{-5}$  for an SNR range of 0=10 dB [4]. Typically, the error drops as a function of the iterative decoding in several error detection and correction coding techniques [5]. One of the most effective error detection and correction mechanisms in this regard is the recursive turbo codes [6]-[7]. This category of codes show high adherence to the Shannon's limit [8]-[9]

The turbo encoding mechanism is typically described by the following attributes [10]:

- 1) Encoder
- 2) Decoder
- 3) Channel
- 4) Interleaver
- 5) De-interleaver
- 6) Recursive block

The encoding mechanism is depicted in figure 3.

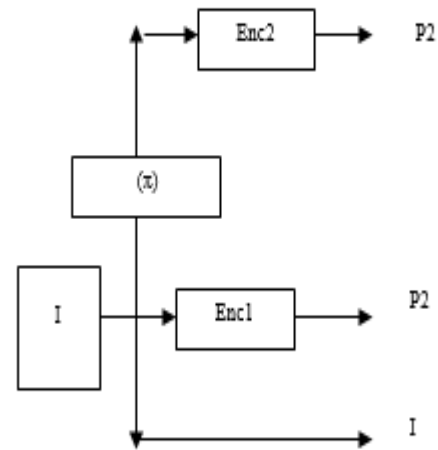


Fig.3 Turbo encoder

The turbo encoder is characterized by:

Input bits.

Parity bits

Here,

I represents the information bits

Interleaver  $\pi$

Encoders

The encoding mechanism is typically performed in a way so as to enhance the reliability of the system [11]. This happens due to the fact that the encoder has three bits as the output for one bit as the input. The encoders are typically symmetric in nature or even asymmetric based on the type of encoder design [12]-[13]. The information bit shared is then passed on to render 3 bits which are [14]:

- 1) Same unaltered bit.
- 2) Encoded bit (P1)
- 3) Encoded bit (P2).

The difference among the bits P1 and P2 lie in the fact that both the bits are distinguished by the act of the interleaver. While the information bit ' I ' directly goes to the encoder 1, the other encoder receives a modified version of the information bit [15]. The two encoders may or may not be similar. In case both exhibit a similar structure, the encoding is termed as symmetric encoding [16].The role of the interleaver is exemplified in the next section.

## II. INTERLEAVING AND PUNCTURING

The interleaving mechanism is fundamentally derived so as to reduce the burst errors in a network [17]. This can be understood through the following diagram.

Transmitted Bits	B0	B1	B2	B3	B4	B6	B7
	1	0	1	0	1	0	1
	1	1	0	1	0	1	10
Received Bits	B0	B1	B2	B3	B4	B6	B7

Fig.4 Burst Errors

The interleaving mechanism is fundamentally used to circumvent the domino effect of errors [18]. This can be seen from figure 4. As there is a missing bit in bit location 2, there is an error in bit 2 which is received by the receiver. The error progresses as the receiver doesn't have cognizance of the transmitters bits. This leads to a cascading progression of the bits and hence the error in one bit results in the errors in other multiple bits. This however can be mitigated in case, the error propagation mechanism is stopped [19]. The exact is done by the interleaver as the interleaver combines the bits into chunks and separates the correlation among the bits. This is however, true only for burst errors with memory and not for random errors [20].

While burst errors are bits which have a cascading effect, the random errors are the errors which can occur at any bit location at any given instance of time [21].

Bit	TX (Y/N)	TX (Y/N)	TX (Y/N)
I	Y	Y	Y
P1	Y	N	Y
P2	N	Y	N
	Time=t1	Time=t2	Time=t3

Fig.5 Puncturing

The puncturing mechanism is based on the planned non-transmission of the bits at some intervals of time. The information bit is not omitted but one of the most common techniques is to omit the parallel transmission of both the

parity bits. This reduces the bit transmission rate of the system [22].

While the original coding rate is 1/3, the new coding rate remains only 1/2. This happens due to the suppression of one bit at a time [23].

### III. TURBO DECODING

The major challenges with error detection and correction for IoT networks are [24]:

1. IoT networks are prone to noise and disturbance effects causing increase in bit error rate of the system. This decreases the reliability and trustworthiness of the system.
2. Often IoT networks are resource constrained in terms of memory and processing power. Hence coding techniques with relatively low computational complexity in terms of number of iterations are needed.
3. Lesser iterations are also needed to minimize the latency (delay) of the system as IoT networks can be used for time critical applications.
4. There exists a fundamental trade off between the number of iterations and Bit Error Rate (BER) of the system where higher iterations would result in lower BER but would significantly increase the system's latency and complexity.

Typically two decoders are employed for decoding in the cascading manner [25]. The BCJR based algorithm is used for the decoding of the codes.

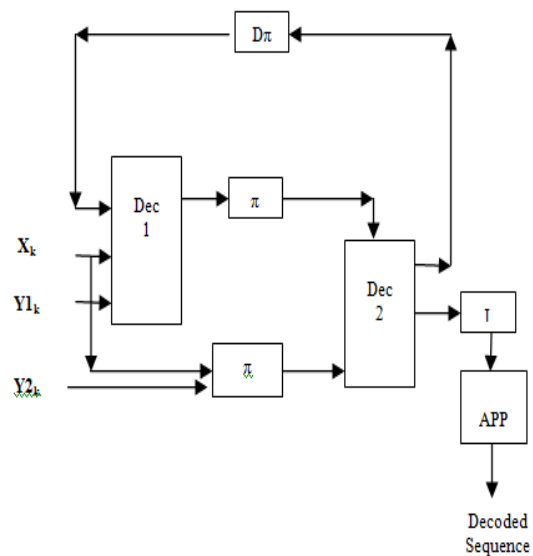


Fig.6 The turbo decoding mechanism

The figure above depicts the block diagram of the turbo decoder which comprises of two decoders. The interleaver is represented by  $(\pi)$  and the de-interleaver is represented by  $(D\pi)$ . The decoding process is done in a manner which incorporates both the decoders which are designated as D1 and D2. The information bit I and one of the parity bits is fed to decoders 1 and 2 respectively. Each of the decoders surmise the output based on the input information received, and the verdict of the other decider [26]. Thus the feedback loop connects decider 1 and decoder 2's outputs in a recursive manner in which the iterative process takes place in the decoding mechanism. At the beginning of the decoding process, the output of any one of the decoders is considered to be equi-probable probabilities of 1 or zero occurring. However, the final bit pattern is considered at the output terminal of D2 [27].

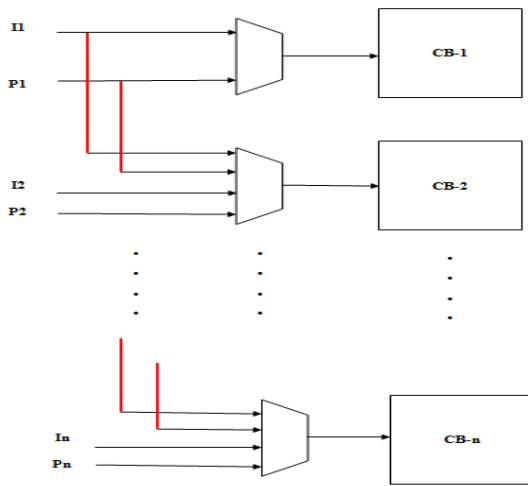


Fig.7 The proposed approach

In the proposed approach, both information and parity bits are coupled. Previous approaches do not have a method to couple both I & P.

In the proposed scheme, the information bits are designated by I and the interleaved bits are denoted by P. In this case, the n code blocks (CB) constitute a transport block (TB). The transport block vector (T) is segmented into 'n' code blocks

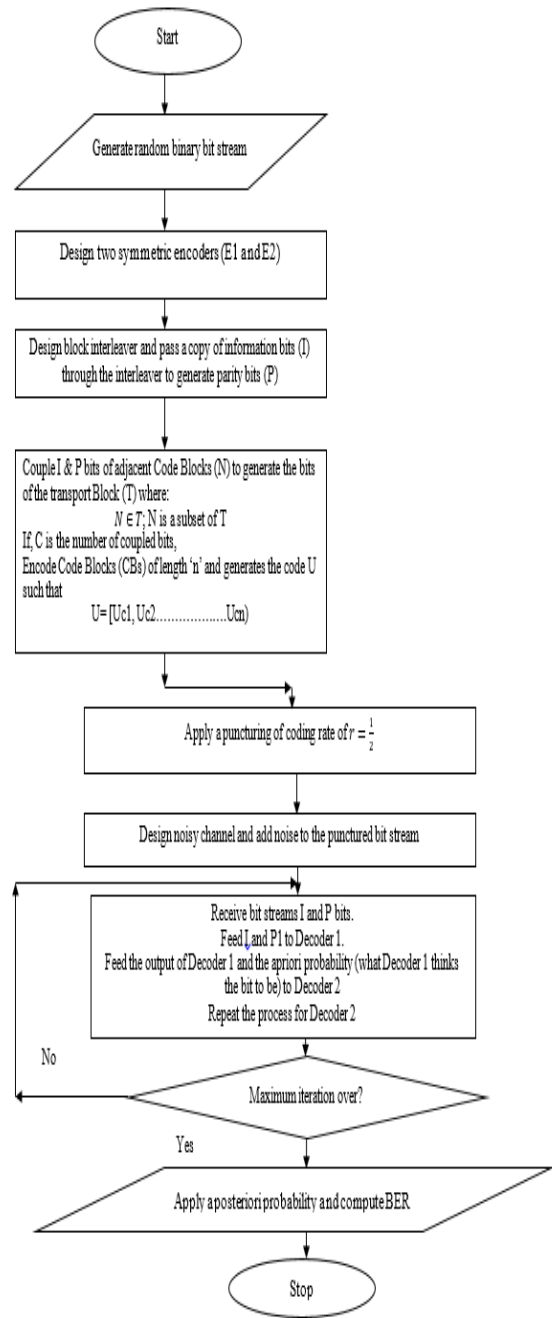


Fig.8 Proposed Flowchart

Figure 8 depicts the flowchart of the proposed system. The flowchart represents the sequential steps to implement the proposed system.

#### IV. EXPERIMENTAL RESULTS

To The system has been designed on MATLAB 2020a. To emulate the actual data streams generated by a multitude of devices in an IoT network, random binary data has been generated.

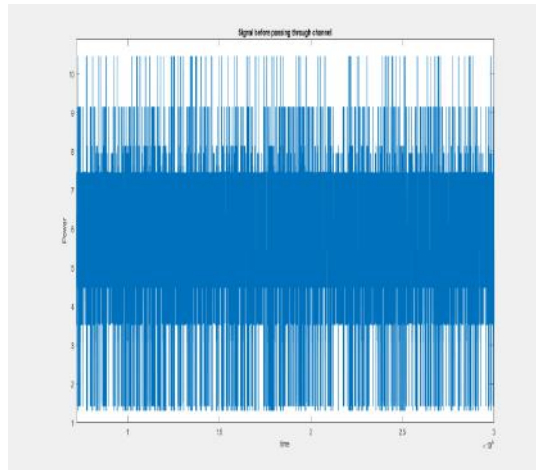


Fig.9 binary bits

Figure 9 depicts the binary data stream generated to emulate random binary data transmission.

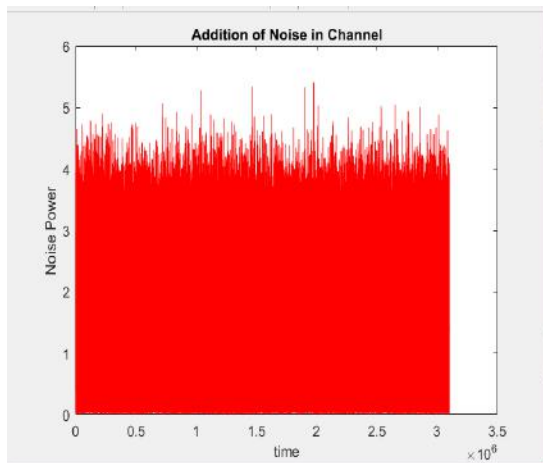


Fig.10 Addition of disturbance

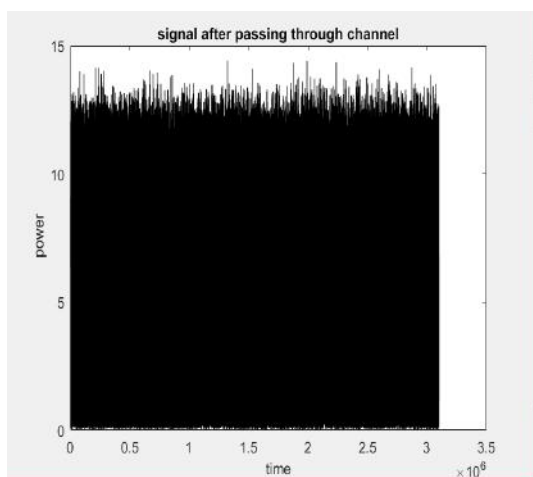


Fig.11 Effect of noise addition.

Figure 10 depicts the addition of noise in the wireless channel. Random noise has been added so as to replicate the channel conditions in an actual IoT network. The random fluctuations in the noise as a function of time has been shown in the figure.

The effect of noise addition on the binary data stream in the time domain has been depicted in figure 11. It can be seen that the binary data stream has been manipulated by the addition of noise.

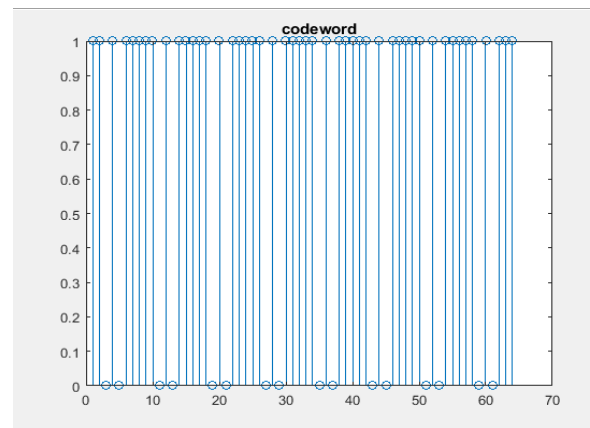


Fig.12 Formation of the turbo Code-word

Figure 12 depicts the binary code-word generated by the proposed system. The binary representation of the code word has been shown.

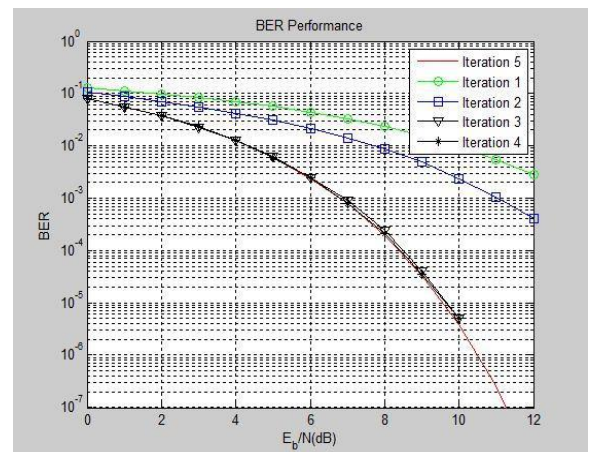


Fig.13 error as function of iterations.

Figure 13 depicts the bit error rate of the proposed system as function of iterations. It can be observed that as the iterations increase, the BER of the system continuously plummets. To represent the signal strength for binary data, the term energy per bit  $E_b$  has been used.

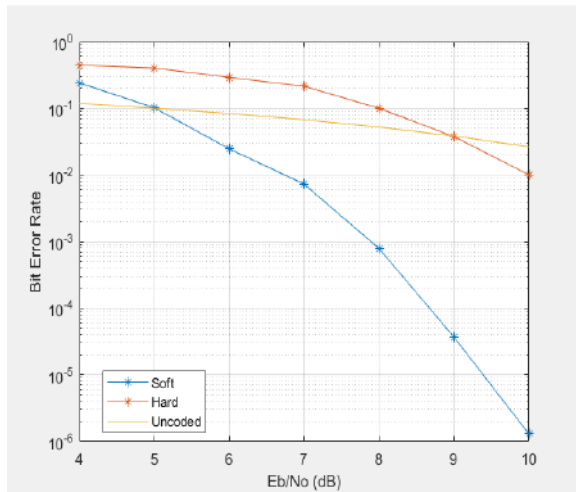


Fig.14 Coded and un-coded error rates

Figure 14 depicts the comparative analysis of the un-coded, hard coded and soft coded (Turbo) versions of binary transmission for the system. It can be clearly observed that the soft turbo coded probabilistic approach attains the steepest fall in the error rate compared to the hard coded and un-coded counterparts.

## V. CONCLUSION

Internet of Things (IoT) networks are finding applications in different domains such as automation, climate monitoring, defense etc. However, due to the wireless medium of the nature, noise and disturbance effects cause increase in the bit error rate of the system thereby causing low reliability and trustworthiness. The essence of the turbo coding mechanism lies in the fact of steep fall in errors near the relatively low SNR values. The proposed system implements coupling of both I and P bits in adjacent code blocks. To recreate a practical IoT scenario, noise is added to the bit stream. The experimental results are gauged in terms of the iterations to attain low values of the errors for the low Shannon range SNR. The BER obtained by the proposed system is  $10^{-7}$  which is significantly less than the BER of the previous system  $10^{-5}$  [1]. Thus it can be concluded that that the proposed system outperforms existing work in terms of the bit error rate (BER) which is the predominant metric for system reliability and trustworthiness.

## REFERENCES

[1] S. Zhao, J. Wen, S. Mumtaz, S. Garg and B. J. Choi, "Spatially Coupled Codes via Partial and Recursive Superposition for Industrial IoT With High Trustworthiness," in *IEEE Transactions on Industrial Informatics* 2022, vol. 16, no. 9, pp. 6143-6153.

[2] Chaofan Chen, Li Li, Li Wang, Shuai Wang, Xiangming Li, George K. Karagiannidis, "Noncoherent Detection With Polar Codes", *IEEE* 2021.

[3] Saeedeh Moloudi, Michael Lentmaier, Alexandre Graell i Amat, "Spatially Coupled Turbo-Like Codes", *IEEE* 2020.

[4] Ritesh Nagar, S. K. Bhatt, "A Comparative analysis of a Conventional and cross phase UPQC for enhancing the Power Quality," vol. 7, no. 7. *IJSHRE*, 2018.

[5] Suihua Cai, Nina Lin, and Xiao Ma, "Block Markov Superposition Transmission of BCH Codes with Iterative Erasures-and-Errors Decoders", *IEEE* 2019.

[6] Gianluigi Liva, Lorenzo Gaudio, Tudor Ninas and Thomas Jerkovits, "Code Design for Short Blocks: A Survey", *IEEE* 2018.

[7] Erdal Arkan, Daniel J. Costello, Jr., Joerg Klierer, Michael Lentmaier, Paul Siegel, Ruediger Urbanke, Michael Pursley, "Guest Editorial Recent Advances in Capacity Approaching Codes", *IEEE* 2017.

[8] Boulat A. Bash, Dennis Goeckel, Saikat Guha, Don Towsley, "Hiding Information in Noise: Fundamental Limits of Covert Wireless Communication", *IEEE* 2015.

[9] Zunaira Babar, Soon Xin Ng and Lajos Hanzo, "EXIT-Chart Aided Near-Capacity Quantum Turbo Code Design", *IEEE* 2015.

[10] Michael Lentmaier, Saeedeh Moloudiy, and Alexandre Graell i Amat, "Braided Convolutional Codes – A Class of Spatially Coupled Turbo-Like Codes", *IEEE* 2014.

[11] Tsung-Yi Chen, Kasra Vakilinia, Dariush Divsalar, and Richard D. Wesel, "Protograph-Based Raptor-Like LDPC Codes", *IEEE* 2014.

[12] A. Amat S. Moloudi and M. Lentmaier, "Spatially coupled Turbo codes: Principles and finite length performance," *IEEE 11th ISWCS*, pp. 883–887, 2014.

[13] T. Breddermann and V. Peter, "Rate-compatible insertion convolutional Turbo codes: Analysis and application to LTE," *IEEE Trans. Wireless Comm.*, vol. 13, no. 3, pp. 1356–1366, Mar. 2014.

[14] K Niu, K Chen, JR Lin, "Beyond turbo codes: Rate-compatible punctured polar codes", *IEEE* 2013

[15] MM Wilde, MH Hsieh, Z Babar, "Entanglement-assisted quantum turbo codes," *IEEE* 2013

[16] G Liva, E Paolini, B Matuz, S Scalise, "Short turbo codes over high order fields," *IEEE* 2013

[17] K Anwar, T Matsumoto, "Accumulator-assisted distributed turbo codes for relay systems exploiting source-relay correlation", *IEEE* 2012

[18] K Niu, K Chen, "CRC-aided decoding of polar codes", *IEEE* 2012

[19] SH Lee, JK Kwon, "Turbo code-based error correction scheme for dimmable visible light communication systems", *IEEE* 2012

[20] T. Breddermann and P. Vary. "EXIT functions for parallel concatenated insertion convolutional codes," *IEEE*, 2011.

[21] MM Wilde, MH Hsieh, "Entanglement boosts quantum turbo codes", *IEEE* 2011

[22] G Liva, S Scalise, E Paolini, "Turbo codes based on time-variant memory-1 convolutional codes over  $F_q$ ", *IEEE* 2011

- [23] QT Dong, M Arzel, C Jego, Stochastic decoding of turbo codes:, IEEE 2010
- [24] M Cluzeau, M Finiasz, JP Tillich, Methods for the reconstruction of parallel turbo codes, IEEE 2010
- [25] A. Jangid and P. Chauhan, "A Survey and Challenges in IoT Networks," 2019 International Conference on Intelligent Sustainable Systems (ICISS), 2019, pp. 516-521.
- [26] R. G. Maunder, "A Fully-Parallel Turbo Decoding Algorithm," in IEEE Transactions on Communications, 2015, vol. 63, no. 8, pp. 2762-2775.
- [27] Y. Jiang, S. Kannan, H. Kim, S. Oh, H. Asnani and P. Viswanath, "DEEPTURBO: Deep Turbo Decoder," 2019 IEEE 20th International Workshop on Signal Processing Advances in Wireless Communications (SPAWC), 2019, pp. 1-5.
- [28] P Durga, B Yamuna, P Salija, Implementation of low complex SOVA in GNU radio, Procedia in Computer Science, Elsevier 2018, vol. 143, pp.876-885.

# Fire detection algorithm based on the fusion of YOLOv8 and Deformable Conv DCN

Lin Po Shang<sup>1</sup>, Yan Zuo Chang<sup>2,\*</sup>, Yi Chen<sup>1</sup>, Yong Shan Ou<sup>3</sup>

<sup>1</sup>Department of Energy and Power Engineering, Process Equipment and Control Engineering major, Guangdong University of Petrochemical Technology, China

<sup>2</sup>Department of Energy and Power Engineering, Guangdong University of Petrochemical Technology, China

<sup>3</sup>Department of Electronic Information Engineering, Electronic Information Science and Technology major, Guangdong University of Petrochemical Technology, China

\*Corresponding author: [ros1517877219@outlook.com](mailto:ros1517877219@outlook.com)

Received: 29 Jun 2024,

Receive in revised form: 31 Jul 2024,

Accepted: 08 Aug 2024,

Available online: 15 Aug 2024

©2024 The Author(s). Published by AI  
Publication. This is an open-access article  
under the CC BY license  
(<https://creativecommons.org/licenses/by/4.0/>).

**Keywords**— *Fire identification, Deep learning, YOLOv8, Deformable Conv*

**Abstract**— *With the progress of fire monitoring and Coping technique, image recognition based on deep learning has shown great potential in the field of fire detection. Aiming at the accuracy and efficiency problems existing in the existing object detection algorithms, this study proposed an improved YOLOv8 algorithm to improve the real-time recognition capability in the fire scene. Through experimental verification on standard fire data sets, this study evaluated the detection performance of the improved YOLOv8 algorithm fused with Deformable Conv. The experimental results show that the improved YOLOv8 has improved the fire identification accuracy compared with the traditional version, and has certain potential for practical application in fire monitoring system.*

## I. INTRODUCTION

In modern society, fire occurs everywhere and crises abound, and almost any environment with heat sources or combustible materials has hidden safety hazards, which seriously affect the living environment of human beings. Human contact with fire may lead to burns of different degrees, ranging from minor surface burns to serious deep tissue damage. Severe burn require long-term medical treatment and may result in disability or life threatening [1]. In addition, fire also has irreversible damage to buildings, production and environment. Fire can cause internal and external burning of buildings, resulting in partial or complete damage to building structures [2]. High temperature can also make building materials lose strength such as steel and concrete, and even lead to structural collapse, posing a direct threat to the durability and safety of buildings [3]. In large-scale production environments such as warehouse workshops, chemical plants and assembly lines, fire spreads quickly and may cause violent explosions when it comes into contact with flammable and

explosive substances, which damages important equipment in the production environment and threatens personnel's life and property safety [4].

With the rapid development of modernization, warning of fire is particularly important in industrial fields and large public places. At present, warning of fire is mainly based on sensors, such as smoke sensors and temperature sensors. Those mainly detect smoke and temperature [5], and the detection range is limited while the effect is difficult to guarantee. When the smaller flame appears, it is generally not immediately detected and reflected in time, which is often the cause of fire in the production workshop or chemical plant. The current development of AI technology is rapidly advancing, especially with breakthrough achievements in the field of mechanical learning. Computer vision technology is an application field of mechanical learning. In recent years, computer vision technology has had a mature development and has been applied in all walks of life, especially in the field of target detection and recognition. With the improvement of

technology, its accuracy and detection speed continue to improve. Instead of relying on sensors and manual inspection to prevent disasters, we proposed an improved visual recognition algorithm based on convolutional neural network (CNN) for fire detection in this paper.

At present, there are many kinds of object detection technologies. Compared with traditional object detection algorithms, the recognition algorithm based on convolutional neural network (CNN) has more advantages, which can not only better characterize complex features, but also greatly improve the accuracy and real-time performance. It is widely used in vehicle detection and recognition [6], automatic driving [7], attitude detection, fault diagnosis of manufacturing equipment and robot fields [8, 9]. Currently, the two main object detection algorithms based on convolutional neural network (CNN) are One-stage object detection algorithm and two-stage object detection algorithm. The detection process of two-stage detection algorithm is divided into two parts, as shown in Figure 1: (a) two-stage object detection algorithm and (b) single-stage object detection algorithm.

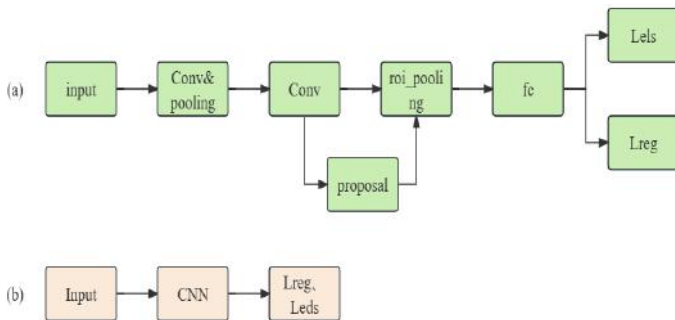


Fig. 1: Comparison between two-stage object detection algorithm and single-stage structure

First of all, we generate the candidate region, and then determine whether there is an object to be detected in the candidate region, and the category of the object. At present, the most popular Two-stage algorithm is R-CNN series, including R-CNN, SPP-Net, Faster-CNN, etc. [10]. Compared with Two-Stage algorithm, One-Stage algorithm carries out single regression and reduces Anchor steps. The category and location information is given directly through the Backbone network, so it is faster and easier to learn the generalization characteristics of the target, reducing the generation of false positive. The SSD and YOLO series are the mainstream of One-Stage. In 2016, Joseph Redmon et al. proposed a one-stage object detection network [11], which has a very fast detection speed and can process 45 frames of pictures per second. The author named it You Only Look Once, and the first generation of YOLO was born. With the subsequent in-depth research, YOLOv2 and YOLOv3 have been come out one after another, which have strong migration ability

and are widely used in various fields. In terms of risk detection, YOLO has also played its role. Ying Liu developed a risk identification system in oil field production environment based on YOLOv3 [12]. Zizqiang Li et al. applied YOLOv5 in the intelligent detection of unsafe conditions on the construction site [13], Ruiguo Wei used YOLOv5 to develop a fire image recognition method [14], and Qingxu Li designed the cabin fire detection system with an improved YOLOv5 algorithm [15]. This study focused on the 8th generation YOLO algorithm (YOLOv8) is proposed an improved vision detection algorithm based on convolutional neural network (CNN) fused with Deformable Conv for fire identification.

## II. INTRODUCTION OF YOLOv8 NETWORK ARCHITECTURE

YOLOv8 is a new generation of target detection algorithm launched by ultralytics. It is an innovation and improvement made by ultralytics team on the basis of YOLOv5 previously launched [16]. On the basis of inheriting the real-time detection characteristics of YOLO series, the model structure has been comprehensively optimized and improved to elevate the performance of the model. Its network structure diagram is shown in Figure 2.

Its general architecture is basically composed of Input, Backbone, Neck and Head. Compared with YOLOv5, the first layer convolution size of Backbone is changed from the original 6×6 to 3×3, and C3 module is changed into Cf2 module [17], which uses the relevant structure in YOLOv7. This part is replaced by multiple cross-layer connections instead of one convolutional module and one skip module, and the split part is added, which is based on

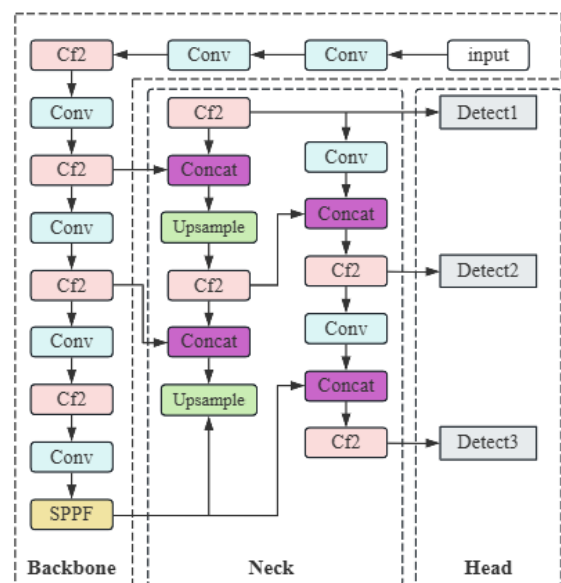


Fig. 2: YOLOv8 network structure diagram

the part of YOLOv7. The replacement helps the network to understand the characteristics of different scales, improving its accuracy and robustness. Neck, as an intermediate layer, fuses with the transmitted features of backbone, which is conducive to improving performance. While YOLOv8 replaces C3 module in Neck with Cf2 module, the original 1×1 convolution is removed [18].

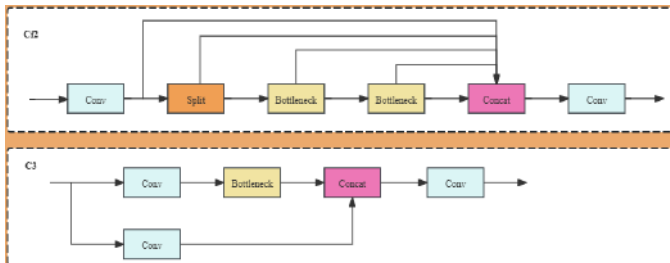


Fig. 3: Comparison between C3 module and C2f module

The Head is mainly responsible for generating the final target detection results from the features extracted by the Backbone network, helping to identify and locate various targets in the input image. Compared with Yolov5, the Coupled Head was changed to a similar to the Decoupled-Head structure. [19] As shown in Figure 3, the regression branch and prediction branch were separated.

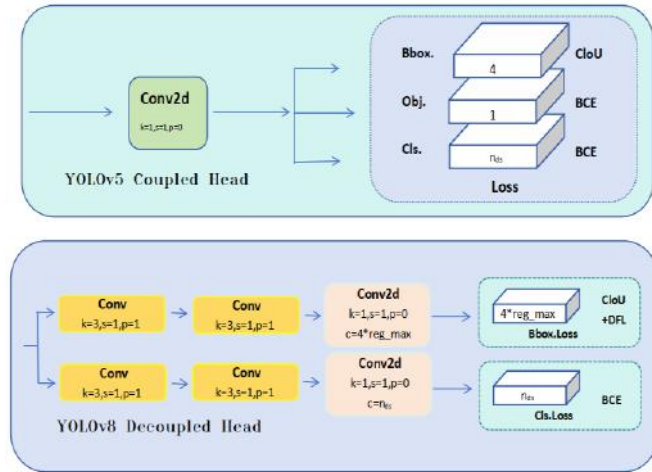


Fig. 4: Comparison between YOLOv5 and YOLOv8 Head

The original detection head was divided into multiple subtasks, each of which was responsible for detecting targets of related undetermined categories. This approach can improve the scalability and flexibility of the model, which is conducive to processing. This approach can improve the scalability and flexibility of the model, which is conducive to processing multiple types of detection targets, and optimize each related subtask to improve the accuracy of detection. This improvement can also make the model better adapt to different application scenarios

and target categories, and cope with the structure of different detection layers by adjusting the number and size of convolutional layer and fully connected layer.

### III. ALGORITHM IMPROVEMENT AND OPTIMIZATION

#### 3.1 Principle analysis of Convolution operation

In the convolutional neural network, a high value or a low value is needed to distinguish the feature region from other regions in order to extract features from the input image data. The process of generating values is called Convolution operation, and the core of the Convolution operation is a small matrix called Convolutional Kernel. This Convolutional Kernel slides over the entire input data to generate an output feature map by weighted summing local regions of the input data. At each step, the Convolutional Kernel is multiplied with a small window of the input data by elements part by part, and then the results are added to obtain a unit value of the output feature map. The sliding window usually moves on the input data by a certain translation unit, and moves a fixed unit distance each time [20]. This process allows the Convolutional Kernel to efficiently detect local features in the input data, such as edges, textures, or other higher-level features. For each input data, the Convolution operation will generate an output feature map, which has the same dimension as the input data in space, but the depth will be different. These feature maps contain different feature information of the input data, which can be used as input for the subsequent neural network layer.

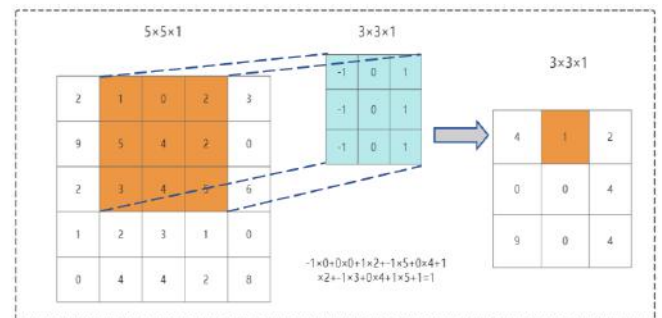


Fig. 5: General convolution process

Figure 5 shows the process of common convolution calculation on the input feature graph. The size of Convolutional Kernel is 3×3, and the size of the input feature graph is 5×5. The weight of the Convolutional Kernel is multiplied by the corresponding position element of the input feature graph, and the value of the output feature graph element is obtained by summing. The rest

of the input matrix is calculated step by step to get the output feature map.

Input any point  $P_0$  on the feature graph, and the convolution process can be expressed as:

$$y(p_0) \sum_{p_n \in R} \omega(p_n) \times x(p_0 + p_n) \quad (1)$$

Where  $P_n$  represents the offset of each point in the Convolutional Kernel relative to the center point, which can be expressed by the following formula (3x3 Convolutional Kernel for example) :

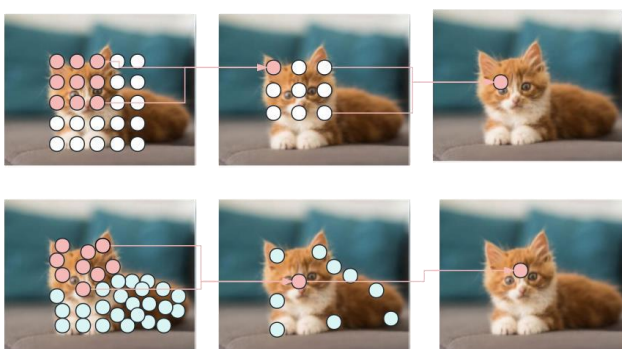
$$R = \{(-1, -1), (-1,0), \dots, (0,0), \dots, (1,0), (1,1)\} \quad (2)$$

We can take the center of the matrix as the origin, and each grid uses a coordinate system to represent the position of that part.  $w(p_n)$  represents the weight of the corresponding position of the convolution check, and this value is generally a constant,  $x(p_0+p_n)$  represents the element value at  $p_0+p_n$  position on the input feature map, and  $y(p_0)$  represents the element value at  $p_0$  position on the output feature map, which is obtained by the relevant convolution operation of the Convolutional Kernel.

### 3.2 Deformable Conv ideas

The Convolutional Kernel of conventional convolution has a fixed size and shape. For more complex image data, it is difficult for conventional Convolutional Kernel to extract more accurate features, especially the edge features of graphics. If Convolutional Kernel can be

adjusted according to the characteristics of input data during convolution operation, the characteristics of data can be better obtained and the detection accuracy can be improved. This is also the core of Deformable Conv.



(top) Standard convolution (bottom) Deformable Conv  
 Fig. 6: Convolution example of standard convolution and Deformable Conv

As can be seen from the upper and lower comparison shown in Figure 6, for this cat image, the features extracted from the standard convolution cured structure

also have a certain curing effect. The collating features extracted from the detected objects in the image may not be obvious, and its rectangular plane arrangement cannot be well correlated with sampling. The sampling position of deforming convolution is more in line with the shape characteristics of the object itself [21], and it has certain elasticity and can better adapt to the boundary conditions of the image. Therefore, after incorporating deforming convolution for convolution operations, the output feature points correspond to the overall features of the data, which can improve the acquisition of useful information of the data and improve the accuracy of the model compared with conventional convolution.

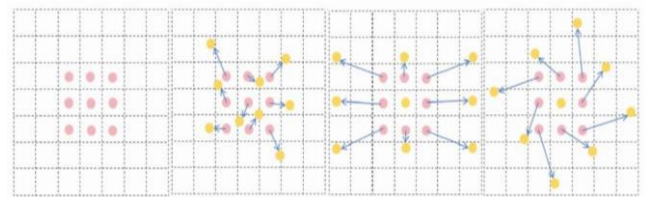


Fig.7: Different adoption points of Deformable Conv

As shown in Figure 7, (a) is the sampling method of a common 3x3 Convolutional Kernel, and (b) is the change of sampling point after Deformable Conv plus offset, where (c) and (d) are special forms of Deformable Conv. The light pink dots represent the 9 sampling points of the conventional square Convolutional Kernel, the light blue arrows represent the offset vector, and the yellow ones represent the offset sampling points. The Deformable Conv introduces an offset for each point based on formula 1, which is generated by the input feature map with another convolution, usually a decimal.

$$y(p_0) \sum_{p_n \in R} \omega(p_n) \times x(p_0 + p_n + \Delta p_n) \quad (3)$$

In the Deformable Conv, the regular grid  $R$  increases the offset  $\Delta p_n$ . Since the position after adding the offset is generally a decimal, it does not correspond to the actual pixel points on the input feature map.

Figure 8 shows the Deformable Conv diagram. It can be seen that offsets are generated by using an additional convolution, which is not a convolution operation. In the figure 8,  $N$  is used to represent the size of the Convolutional Kernel region, for example, the size of a convolution kernel is 3x3,  $N=9$ . The green process in the figure is the process of convolutional learning offset, where the channel size of the offset field is  $2N$  and represents that the Convolutional Kernel learns the offset in the x direction and the y direction respectively.

On the input feature map, the convolution sampling region corresponding to common convolution operations is a square with the size of the Convolutional Kernel, while

the convolution sampling region corresponding to Deformable Conv is some points represented by blue boxes. This is the difference between Deformable Conv and ordinary convolution.

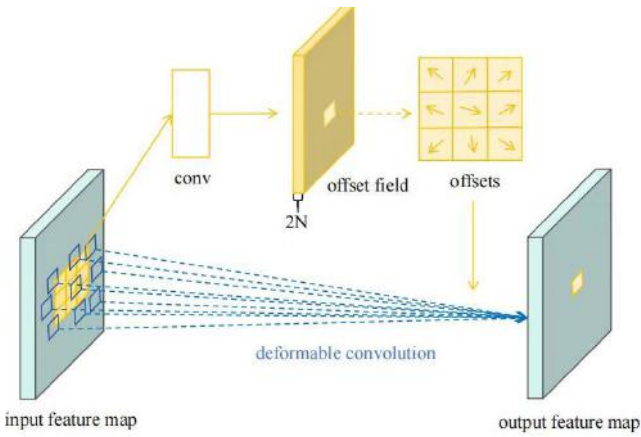


Fig.8: Schematic diagram of Deformable Conv

In terms of the specific details of the corresponding schematic diagram, the size of the convolution sampling area corresponding to a point on an output feature map and the input feature map is  $K \times K$ . According to the operation of Deformable Conv, each convolution sampling point in the  $K \times K$  region must learn a deviation offset. The offset is expressed in coordinates, so an output must learn  $2 \times K \times K$  parameters. If an output size is  $H \times W$ , so a total of  $2 \times K \times K \times H \times W$  parameters must be learned. That is, the offset field ( $N=K \times K$ ) in the preceding figure has the dimensions  $B \times 2 \times K \times K \times H \times W$ , where  $B$  represents batch\_size.

#### IV. EXPERIMENT AND RESULT ANALYSIS

##### 4.1 Experimental environment

The development language of the training model is Python, the compiler is Python3.9.13, the compilation tool is pycharm2023, the deep learning framework Pytorch1.13.0, and CUDA version 11.16. The experiment was carried out in Windows11 operating system. CPU was AMD Ryzen 7 5800H with Radeon Graphics 3.20GHz, and GPU was NVIDIA RTX3060Ti with 16G video memory.

Related images were selected from the network in the experiment, and the data set contained more than 2000 pieces of two types of data. The selected images were annotated by labeling tool in pycharm, and the annotated picture information was automatically converted into YOLO\_txt format. Then the original image and YOLO\_txt format images are divided into training set, verification set and prediction set proportionally.

During the training, Mosaic data was used to enhance the first 95% epoch. During the torch training, the parameter value was Epoch 100, the compressed size of the input image Imageinput  $640 \times 640$ , and the batch size of the training Batchsize 16.

##### 4.2 Evaluation Indicators

In order to verify the improved performance of YOLOV8 model, this experiment verified the selection accuracy P(Precision), Recall R(Recall), Average Precision AP(Average Precision), and average precision mAP(mean Average Precision). Precision-confidence curve and loss line curve were used as evaluation indexes. The calculation of P, R, AP and mAP is as follows: The evaluation indexes in this experiment include accuracy rate, recall rate and average accuracy, and the formula is shown as follows.

$$\text{Precision} = \frac{TP}{TP+FP} \tag{4}$$

$$\text{Recall} = \frac{TP}{TP+FN} \tag{5}$$

$$\text{AP} = \int_0^1 P(R) dR \tag{6}$$

$$\text{mAP} = \frac{\sum_{i=1}^k AP_i}{k} \tag{7}$$

TP (True Positive) indicates the number of Positive classes predicted as positive classes, that is, the number of positive classes predicted correctly. FP (False Positive) indicates the number of negative classes predicted as positive classes, that is, the number of negative class samples predicted incorrectly. The accuracy rate  $P$  represents the proportion of the predicted samples in the positive samples, and the actual proportion of the true positive samples. The recall rate  $R$  represents the proportion of truly positive samples in all predicted samples. While AP is the average accuracy of each category, mAP represents the average AP of multiple categories, and  $m$  is the number of categories. In this detection task, the types of input data are fire and spark, so  $m=2$ .

Compared with the experimental results shown in Figure 9-10, it can be seen that the precision, recall and mAP after the improvement have been improved to varying degrees, indicating that the overall accuracy of the model after incorporating the demorphable convolution has been improved to some extent.

The horizontal coordinate of the graph named Precision-confidence curve represents the detector's confidence, and the vertical coordinate represents the accuracy (or recall rate). The shape and position of the

curve reflect the performance of the detector at different confidence levels. It provides useful information for evaluating the performance of the detector at different confidence levels. It can be seen from this comparison experiment figure that the accuracy of the detector is improved after the use of Deformable Conv. The detector can maintain a low false positive rate while maintaining a high recall rate, and the recognition accuracy of the target is high.

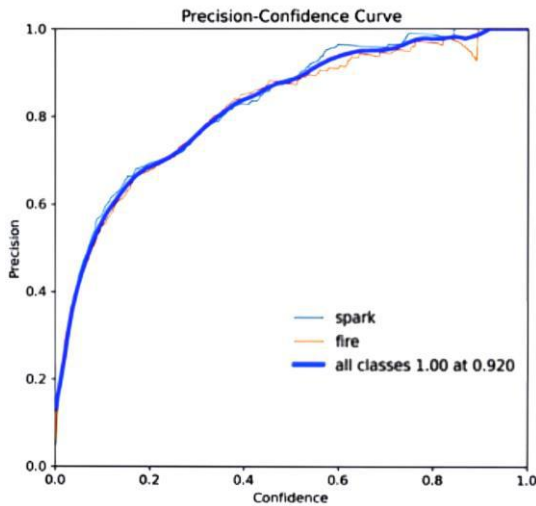


Fig.9: Feedback curve of the improved Precision-confidence curve

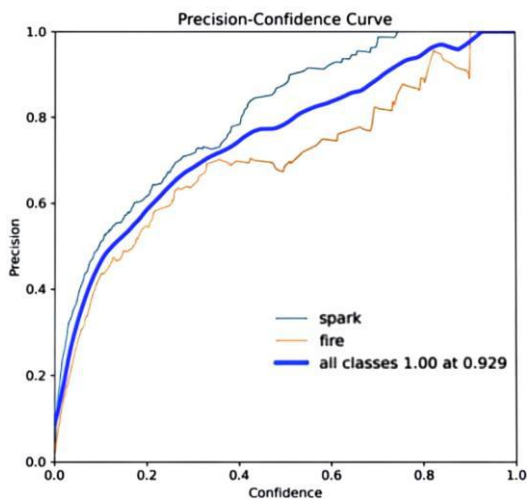


Fig.10: Precision-confidence curve Feedback curve before improvement

Loss function plays an important role in target detection tasks, which is used to measure the difference between the predicted value and the real value of the model. The resulting loss function includes box\_loss (positioning loss), df1\_loss (feature point loss) and cls\_loss (classification loss), as shown in Figure 11-12. Box\_loss is used to calculate the difference between the predicted

bounding box and the real bounding box, and IOU (Intersection overUnion) is used as a metric to measure the overlap between the two bounding boxes. Box\_loss

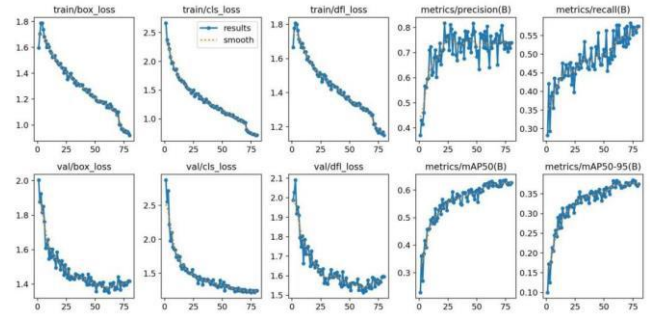


Fig.11: Visual analysis diagram of experimental results before improvement

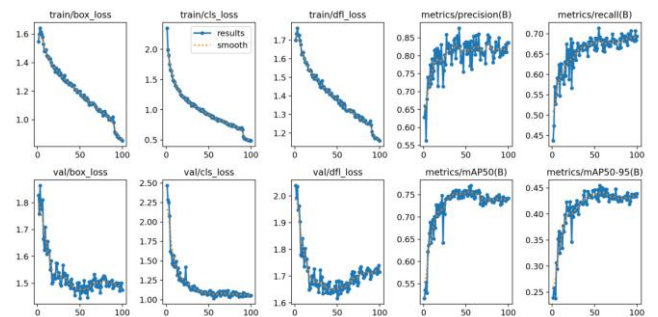


Fig.12: Visual analysis diagram of the improved experiment

calculates the IOU between the predicted box and the real bounding box. By minimizing box\_loss, the model can learn a more accurate boundary box position, and the smaller the value, the more accurate the positioning. It can be clearly seen from image comparison that the improved box\_loss mean is significantly smaller. Cls\_loss is used to calculate the difference between the predicted class and the real class, and Cross Entropy Loss is used to measure the classification accuracy. The loss value of the class is calculated by comparing the difference between the predicted class distribution and the real class label. By minimizing cls\_loss, the model can learn more accurate category classification, and the smaller the value, the more accurate the classification. Through comparison, it can be seen that the mean value of improved cls\_loss is significantly smaller than that of pre-improved cls\_loss, and df1\_loss (feature point loss) is a custom loss function introduced in YOLOv8. YOLOv8 uses feature points to predict the direction and Angle information of the object, which is used to calculate the difference between the predicted feature points and the real feature points. By minimizing df1\_loss, the model can learn more accurate

direction and Angle information of the object, and the smaller the value, the more accurate the feature acquisition. Through image comparison, it can be seen that the mean value of  $dfl\_loss$  in the improved model is smaller than that before the improvement.

The detected training image is shown in Figure 13.



Fig.13: Training image detected

## V. CONCLUSION

All data sets in this experiment were obtained legally from the Internet in terms of model environment construction, relevant data sets construction, model training, and evaluation results. After replacing standard convolution with Deformable Conv, the precision of YOLOv8 detection algorithm is 0.835, which is improved to a certain extent compared with the pre-improvement accuracy of 0.768.  $box\_loss$  (positioning loss),  $dfl\_loss$  (feature point loss) and  $cls\_loss$  (classification loss) as a whole decreased by about 0.2, 0.1 and 0.3, indicating that the improved algorithm has improved the ability to locate objects in images, classify different kinds of images, and acquire features of objects.

In addition to the flame type data, this experiment also selected the complex data with relatively fine features - spark, which is still difficult to detect in the scope of fire prevention. However, from the experimental results, the improved algorithm also has a good normalization ability for spark. Compared with the original algorithm, the improved YOLOv8 algorithm can be applied to various scenes, such as shopping malls, chemical plants and other production environments, and has good accuracy. It also has good adaptability to some image data with not obvious

feature points and enhances the algorithm's ability to extract target features.

## ACKNOWLEDGEMENTS

This work was supported by the Research Funding of GDUPT, Horizon Patrol - Machine Inspection Expert Driven by YOLOV8 Engine (No. 71013513124014).

## REFERENCES

- [1] Xiaohuan Zhan, Junqin Gao&Jile Fu.(2018). Application of brace in the treatment of deep hand burns. Journal of Practical Hand Surgery, 32(1), 86-89.
- [2] Kevin Luo&Iebin Lian.(2024).Building a Vision Transformer-Based Damage Severity Classifier with Ground-Level Imagery of Homes Affected by California Wildfires.FIRE, 7(4).
- [3] Yinghao Shi . (2024). High temperature test and residual compressive strength study of C80 high performance concrete. Shanxi Architecture (15), 100-103.
- [4] Conglin Zhou . (2023). Application of intelligent fire extinguishing technology in chemical fire rescue. Chemical Engineering Management (35), 85-87.
- [5] Gefang Lei, Youlong Wu.(2024). Design of warehouse fire warning system based on Internet of Things technology. Internet of Things Technology (07), 35-38.
- [6] Jin Yuchen&Rona (2019). Improved YOLOv2 vehicle real-time detection algorithm combining multi-scale features. Computer Engineering and Design, 40 (5), 1457-1463
- [7] XinYu Zhang, ZhenHong Zou, ZhiWei Li, HuaPing Liu&Jun Li. (2020). Deep multi-modal fusion technology for automatic driving target detection. Journal of Intelligent Systems (04), 758-771.
- [8] Yufeng Ding, Zhengru Liu&Lei Hu.(2021). Research on PCB test bench for temperature controller based on machine vision and FMEA. Experimental Technology and Management (11), 115-120.
- [9] Huifeng Wang, Hao Du , Rong Gao, Yaxiong Tong Lu Peng, Yu Zhao&He Huang .(2024). A climbing robot system for detecting the apparent diseases of pier and column structures based on visual scanning. China Journal of Highway and Transportation (02), 40-52.
- [10] Wang Yanya. (2022). Review of object detection algorithms based on Two-Stage. Journal of Hebei Academy of Sciences (02), 14-22.
- [11] Joseph Redmon, Santosh Divvala, Ross GirshickAli Farhadi.(2016).You Only Look Once: Unified, Real-Time Object Detection.arxiv.
- [12] Huan Liu.(2023). Implementation of Hazardous Operation Identification System for Oil Field Production monitoring Master (Dissertation, Xi 'an Shiyou University). master
- [13] ZiQiang Li, Lei Ren, Li Liu&ZuoHua Miao.(2023). Intelligent detection of unsafe state in construction site based on YOLOv5 algorithm. Civil Engineering Information Technology (03), 20-26.
- [14] Ruiguo Wei.(2022). Transfer Learning-based Fire image Recognition Method Research Master's degree thesis, Xi 'an Technological University. master

- [15] QingXu Li.(2021). Master's Degree in Cabin Fire Detection System Design based on Improved YOLO Algorithm (Dissertation, Huazhong University of Science and Technology). master
- [16] Zhihong Zhao&Ziye Hao.(2024). Improved YOLOv8 small target detection method for aerial photography: CRP-YOLO. *Computer Engineering and Applications* (13), 209-218.
- [17] Wang, Xueqiu, Gao, Huanbing, Jia, ZemengLi, Zijian.(2023).BL-YOLOv8: An Improved Road Defect Detection Model Based on YOLOv8.*SENSORS*, 23(20).
- [18] Jie Li, Yang Liu, Liang Liu, Bengan Su, Jialong Wei, Guangda Zhou ... & Zhen Zhao . Remote Sensing small target detection based on cross-stage two-branch feature aggregation. *Journal of System Simulation* 1-16.
- [19] Yong Liu , Fengshun LV , Xuecun LI &Shiyu Zuo. Object detection algorithm of remote sensing image based on YOLOv8-LGA. *Optoelectronics · Laser* 1-12.
- [20] Liwei Hu, Zhi Hou, XueTing Zhao, Bing Liu , Chen Chen , Yu He&Ruijie Zhang. Research on improving highway traffic risk prediction model based on traffic accident text mining. *Journal of Southwest Jiaotong University* 1-10.
- [21] CunYi Liao, Yi Zheng, WeiJin Liu, Huan Yu&Shouyin Liu.(2024). Multi-task decoupling and fusion algorithm for automatic driving environment awareness. *Computer Applications* (02), 424-431.

# Change in torsion and strength of wires

Prakash Gawali\*, Amit Kumar Kundu

Acropolis Institute of Technology & Research, Indore, Madhya Pradesh, India

\*Corresponding Author

Received: 15 Jun 2024,

Receive in revised form: 11 Aug 2024,

Accepted: 17 Aug 2024,

Available online: 23 Aug 2024

©2024 The Author(s). Published by AI  
Publication. This is an open-access article  
under the CC BY license

(<https://creativecommons.org/licenses/by/4.0/>).

**Keywords—** Wire drawing, temperature,  
tensile strength, speed.

**Abstract—** The use of high speed in the wire drawing process become very common because of increase in customer demands and production rate. In this work the effect of high speed drawing (30m/sec) on mechanical and technological properties of high carbon steel wire has been investigated. Wire rod 5.50mm from steel grade 0.45% carbon and 0.56% carbon were drawn to 1.35mm in 13 draws and two speeds 10m/sec and 30m/sec. After each draw the following properties were determined; tensile strength ( $T_s$ ), temperature ( $T$ ), number of twists ( $N_t$ ), number of bends ( $N_b$ ). A large drop in the number of has been observed for final wires because of increased draw speed. However, there is also an advantage as the wire surface is much smoother after drawing at high speed than at low speed. The results were practically and statistically estimated.

## I. INTRODUCTION

In the wire drawing process, the cross section is reduced by the pulling it through a conical die which is inserted in the die box and the wire is pulled by cylindrical drum which is run by electric motor [1].

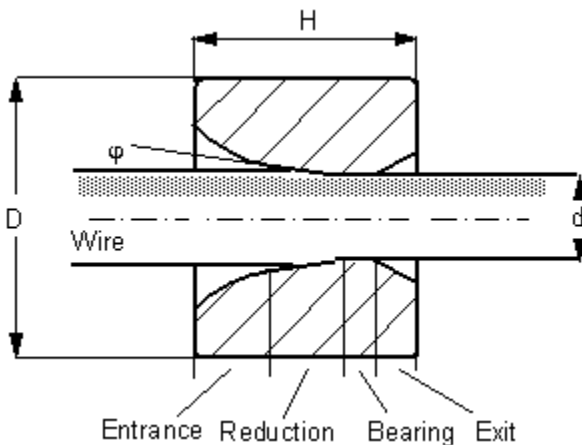


Fig. 1: Area reduction in wire drawing

The major variables in the drawing process are reduction in cross sectional area, die angle, friction along the die work piece interfaces and drawing speed. For successful drawing operation, careful selection of the

process parameters should be carried out. The drawing speed depends on wire material as well as reduction in area for high drawing speeds[2], the heat generated does not have sufficient time to dissipate and a substantial rise in the temperature [3, 4] occurs which has detrimental effect on the quality of product.

Wire drawing operations employing high area reduction and improved lubrication and friction conditions not only save energy, but also reduce production cost by avoiding intermediate passes and annealing operations [5].

Heat generation in wire drawing was first addressed by Siebel and Kobitzsch. [6]. An early refinement of this analysis was made by Korst.[7]. The approach is still widely used today in estimating the temperature rise in wire drawing. While the model predicts that the maximum temperature rise in wire varies with the square root of the drawing speed. It has been observed in experiments to vary linearly with the drawing speed[5]. As well as the cube root of the speed [8]. More recently, this temperature rise was observed to be independent of drawing speed.[9]

Intensifications of the drawing process can be achieved by an increase of a single and a total reduction or by an increase of a drawing speed. However, in practical, technical and economical advantages with a faster speed

are remarkable higher than during drawing with maximum reductions because a higher drawing speed increases the production yield for a specific drawing machine. There has been a trend in wire manufacturing to using high-speed multi hole drawing systems. This application is very important for further industry development but at the same time it is necessary to know the effect of this type of process of not only for the mechanical properties of the drawn wires, but also the factors such as die wear,

lubricant section, die cooling of the dies, drawing drums and others.

### Experimental procedure

The material used to the investigation was rise rod about diameter 5.50mm of low carbon steel after TRIP type heat treatment. The chemical composition of used steel in the investigation is presented in table 1.

Table 1: The chemical composition of TRIP steel

Mass contents in %								
C	Mn	Si	P	S	Cu	Ni	Mo	Sn
0.45	1.40	0.80	0.01	0.07	0.025	0.01	0.006	0.004
0.56	1.30	0.70	0.015	0.08	0.020	0.01	0.004	0.004

Table 2: The volumetric phase contain

Phase contain			
Ferrite, %	Bainite, %	Retained austenite + ~Martensite <sup>1</sup> , %	Retained austenite <sup>2</sup> , %
68.3	15.8	7.5	7.9

After heat treatment and metallographic investigation which confirmed used TRIP type structure, TRIP steel wires drawn in 13 drafts with different drawing speed from diameter 5.5mm to 1.35mm by using classical die with

sintered carbides about angle  $2\alpha = 12^\circ$ . In table 3, the main parameters of drawing process are shown, where: V – drawing speed, A – medium single draft, A<sub>t</sub> – total draft in percentage.

Table 3: The parameters of drawing process

Variant	Drawing machine	Carbon %	V, m/s	Drafts number	A%	At%
A	BB-8	C – 45	8	13	20	93.98
B	BB-8	C- 45	25	13	20	93.98
A	BB-8	C – 56	8	13	20	93.98
B	BB-8	C – 56	25	13	20	93.98

In order to estimate the influence of drawing speed on mechanical properties of wires with TRIP effect, described relation between tensile strength T<sub>s</sub>, Temperature T in °C uniform elongation in total draft function for wires drawn according to variant A (V= 8 m/s), B(V = 25m/s).

For better estimation of the influence of drawing speed on properties TRIP steel wires in the work, modeling of wire drawing process (in Drawing 2D program) has been carried out. It has been estimated:

temperatures, non-dilatation strain and internal stresses drawn wires. Used in program model multi passes drawing (with a few following after themselves single draft) allows to dissolve coastal task with the range of theory of temperature and tensile strength by the variation of the carbon and speed

Table 4: Schedule of draws and mean values of mechanical and technological properties of wires of steel C45. Draw speed 30m/s. and 10m/s.

V= 30m/s C 45									
L <sub>p</sub>	φ	A <sub>p</sub>	A <sub>t</sub>	T <sub>s</sub>	T	E <sub>l</sub>	C <sub>t</sub>	N <sub>b</sub>	N <sub>t</sub>
	(mm)	(%)	(%)	(MPa)	°C	(%)	(%)		
1.	5.50	0.0	-	793	-	8.7	43	14	13
2.	4.91	20	20	872	99	2.6	21	13	14
3.	1.80	20	89.29	1626	239	1.8	53.4	13	28
4.	1.63	20	91.22	1705	250	1.4	52.6	11	30
5.	1.49	20	92.68	1783	261	1.6	51	11	32
6.	1.35	20	93.98	1852	274	1.7	48	10	34
V= 10m/s C 45									
1.	5.50	0.0	-	793	-	8	44	14	13
2.	4.91	20	20	867	94	3	48	13	15
3.	1.80	20	89.29	1600	235	2	51	13	32
4.	1.63	20	91.22	1650	242	2.1	53	12	34
5.	1.49	20	92.68	1757	250	1.8	50	12	36
6.	1.35	20	93.98	1820	260	1.7	48	11	40

Table 5: Schedule of draws and mean values of mechanical and technological properties of wires of steel C71. Draw speed 25m/s. and 8m/s.

V= 30m/s C 56									
L <sub>p</sub>	φ	A <sub>p</sub>	A <sub>t</sub>	T <sub>s</sub>	T	E <sub>l</sub>	C <sub>t</sub>	N <sub>b</sub>	N <sub>t</sub>
	(mm)	(%)	(%)	(MPa)	°C	(%)	(%)		
1.	5.50	0.0	-	1038	-	8	46.8	13	12
2.	4.91	20	20	1117	114	2	19.7	12	13
3.	1.80	20	89.29	1871	253	1.8	53.5	12	26
4.	1.63	20	91.22	1950	254	1.5	51.8	11	28
5.	1.49	20	92.68	2018	264	1.6	51.4	10	30
6.	1.35	20	93.98	2097	276	1.7	47.3	9	32
V= 10m/s C 56.									
1.	5.50	0.0	-	1038	-	8.7	46.8	13	12
2.	4.91	20	20	1062	108	2.8	50.7	13	14
3.	1.80	20	89.29	1792	221	2.3	53.9	13	30
4.	1.63	20	91.22	1870	238	2.1	53.2	12	32
5.	1.49	20	92.68	1956	242	1.7	50.1	11	34
6.	1.35	20	93.98	1980	256	1.8	48.1	10	36

φ = Wire diameter in mm

A<sub>p</sub> = Area reduction per pass in %

A<sub>t</sub> = Total area reduction in %.

T<sub>s</sub> = Tensile strength, MPa.

T = Temp. rise in °C in each pass.

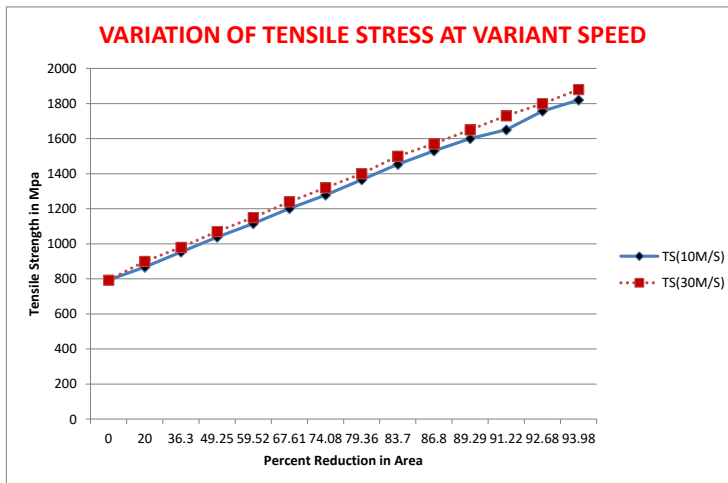
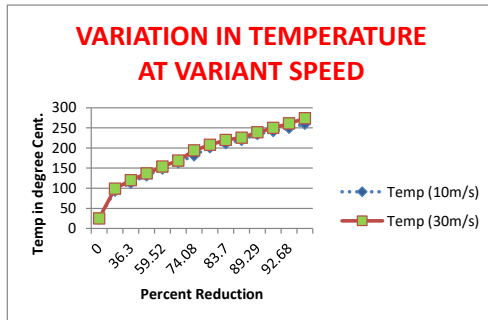
E<sub>l</sub> = Total elongation %.

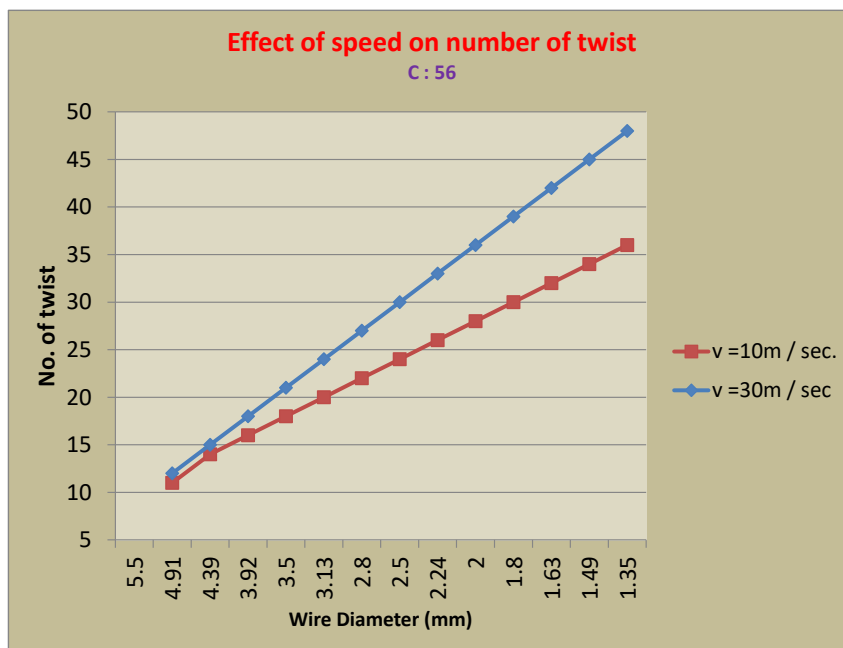
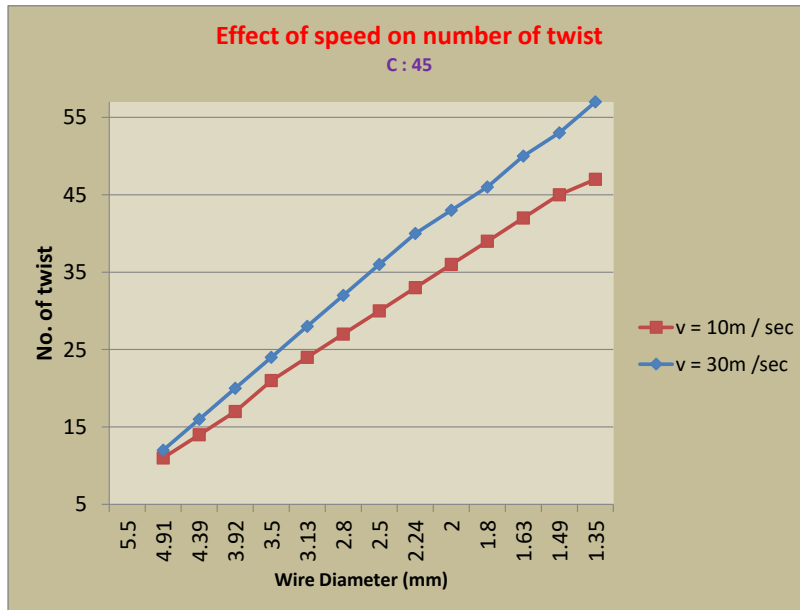
C<sub>t</sub> = Total contraction%

**II. RESEARCH RESULTS: WIRE PROPERTIES**

The wire rod were examined at Tata steel plant for the following properties: tensile strength ( $T_s$ ) in MPa, total elongation ( $E_l$ ) in %, contraction ( $C_l$ ), number of twists  $N_t$ , Number of bends  $N_b$ . The mean values in the table were calculated for the mechanical properties of the 1.35mm wire drawn from the 5.5mm wire rod (steel C 45) at two draw speeds (10m/s and 30m/s). Table 5 shows the same values for the wire drawn from the 5.5mm wire rod (C-56) at draw speeds (10m/s to 30m/s).

The following parameters were calculated for each draw: average temperature on the cross section of the wire ( $T$ ), wire surface temperature ( $T_i$ ). Table 4 shows the value of calculated parameters for all draws with a speed 10m/s for steel C45 at a speed of 30m/s. Table 5 shows the value of  $A$ ,  $A_t$ ,  $T_s$ ,  $T$ ,  $N_b$ ,  $N_t$  for all draws for steel C56 at a speed of 10m/s and 30m/s in the final. The wire surface was observed with an optical microscope at the magnification of 400x.





On the base of a preliminary analysis of data from tables 1-4 and others, it has been decided that process parameters and mechanical properties of tested wires will be estimated for all initial draws, three final draws and last one. This will be helpful in precisely estimating the effect of the draw speed on the above mentioned features of the process and wires ,it can be stated that value of draw stress component in the initial group of draws are independent of a draw speed( for given steel grade). Also that they increase for the final three draws and are highest for the

last draw. The calculated values of this draw stress component for test wires made from steel C45 are lower than those made from steel C56. A similar relationship can be seen for the frictional component of draw stress. In general, the contribution of the friction component in a draw stress is smaller than that for a deformation one.

Regarding the effect of draw speed on temperature of a wire surface, Table 4 and 5 shows that it is similar at a slow draw speed, 10m/s, for all three groups of analyzed draws for steel C45. The result, respectively

are: draws (1-10) 100 - 140°C, draws (11-12) 240 - 250°C and for last draw, 255- 260°C. Drawing at a speed of 30m/s for this same steel, the comparative surface temperatures are : draws (1-10) 100 - 240°C, draw (11-12) 260 - 265°C and for last draw 274 - 276°C. Drawing wires made from the C56 steel resulted in higher surface temperature than for all analyzed wires made from C45 steel, but also in this case for a draw speed of 10m/s the temperature goes on increasing as the carbon percentage increase for draw (1-10) the temperature rise is 10-15°C for draw (11-12) temperature rise is 4-8°C for last draw the temperature rise is 4°C. For a speed of 25m/sec for the considered group of draw the temperature rise for draw (1-10) is 15°C, for draw (11-12) temperature rise is 3-4°C, for last draw temperature rise is 2°C.

Regarding the effect of drawing speed on number of bends, Table 4 and Table 5 shows that the number of bends for draw (1-10) having same value, for draw (11-12) the number of bend decrease by 1, for last draw the number of bend decreased by 1. But as the carbon percentage increases from C45 to C56 the number of bends decreased by 1.

Regarding the effect of drawing speed on the torsion value, Table 4 and Table 5 shows that for C45 as the speed varies from 10m/sec to 30m/sec the torsion value for draw (1-5) increases by 1, for draws (6-13) increases by 2. And as the carbon increases from C46 to C71 the torsion value for draw (1-5) decreases by 1, for draw (6-13) decreases by 2.

Drawing speed was found to have a remarkable effect on tensile strength. The tensile strength in MPa initially having lower value but increases constantly from first pass to last pass. For carbon C – 45, from 793MPa to 1820MPa when the speed is 8m/sec, but tensile strength increases 793 to 1852MPa, when the speed is 30m/sec.

For C – 56 the tensile strength increases from first to last pass 1038MPa to 1870MPa, when speed is 8m/sec and tensile strength increases from 1038MPa to 2097MPa when the speed is 25m/sec.

Thus at high speed and high carbon the value increases by 5 to 10%.

### III. CONCLUSIONS

1. The increase of speed from 8m/sec to 25m/sec caused the increase of tensile strength about 5-6%.
2. The increase of speed causes rise in temperature, which is required to reduce to avoid strain hardening and wire breakage.

3. The increase in speed causes to reduce number of bends by 8-10%. and also as the carbon percentage increase the number of bends goes on decreasing.
4. Higher speed decreases the number of twists observed.
5. At higher speed it is observed that the surface of the wire is smoother than at lower speed.
6. At higher speed the number of bends decreases and it again decreases by increases in the carbon percentage

### REFERENCES

- [1] [http://en.wikipedia.org/wiki/Wire\\_drawing](http://en.wikipedia.org/wiki/Wire_drawing)
- [2] A.K.Lis, J. Lis, Effect of hot deformation and cooling rate on phase transformations in low carbon bainitic steel, proceeding of 11<sup>th</sup> international scientific Conference CAM3S'2005 "Contemporary Achievements in Mechanics, Manufacturing and Material Science" Gliwice – Zakopane 2005, (CD-ROM).
- [3] J.W. Pilaczyk, Z.Muskalski, B Golis, S. Wiewiorowska, M. Sliga, Influence of heat treatment of trip steel wire rod on structure and mechanical properties. Conference Proceedings "Global technologies for Emerging Market's", New Delhi, India 2006, 171-182.
- [4] M. Suliga, Z. Muskalski, the influence of single draft on mechanical-technological properties of TRIP steel wires, Metallurgist-news Metallurgist (2007) 353-356.
- [5] J.Adamezyk., A.Grajcar, heat treatment of TRIP- aided bainitic steel, proceeding of the 11<sup>th</sup> International scientific conference CAM3S'2005' Contemporary Achievements in Mechanics, Manufacturing and Materials Science, Gliwiczakopane2005(CD-ROM).
- [6] A.K. Lis, B.Gajda, Modeling of the DP and trip microstructure in the CMnAlSi automotive steel, Proceeding of the 11<sup>th</sup> International scientific conference CAM3S'2005 "Contemporary achievements in mechanics, manufacturing and the material science", Gliwice-Zakopane 2005, (CD-ROM).
- [7] A. Grajcar, Effect of hot working in the  $\gamma + \alpha$  range on a retained austenite fraction in TRIP- aided steel, journal of Achievements in Materials and Manufacturing Engineering 22/2 (2007) 79-82.
- [8] A. Gajda, A.K. Lis, Thermal processing of CMnAlSi steel at  $(\gamma+\alpha)$  temperature range, Journal of Achievements in Materials and Manufacturing Engineering 18(2006) 355-358.
- [9] P.J. Jacaues, A. Petein, P. Harlet, Improvement of mechanical properties through concurrent deformation and transformation: Newsteels for the 21<sup>st</sup> century, TRIP – International Conference on TRIP aided high strength Ferrous alloys, GRIPS-Proceeding, Ghent (2002) 281-286.

# Development of Intelligent Self-propelled Sprinkler Car Based on Single Chip Computer

Jian-Ting Lai, Yan-Zuo Chang<sup>\*</sup>, Ruo-Yu Yang, Jin-Ping Chen, Man-Lin Zheng

Energy and Power Engineering, Guangdong University of Petrochem Technology (GDUPT), Maoming 525000, China

<sup>\*</sup>Corresponding author

Received: 18 Jul 2024,

Receive in revised form: 15 Aug 2024,

Accepted: 20 Aug 2024,

Available online: 26 Aug 2024

©2024 The Author(s). Published by AI  
Publication. This is an open-access article  
under the CC BY license

(<https://creativecommons.org/licenses/by/4.0/>).

**Keywords**— *self-propelled car; Arduino UNOR3; sprinkle water; follow the trail and avoid obstacles*

**Abstract**— *This paper designs an intelligent self-propelled sprinkler car with Arduino UNOR3 as the control board. The vehicle is equipped with an ATmega328P single chip microcomputer, sensor expansion board, L298N motor drive module, infrared tracking sensor, infrared obstacle avoidance sensor, sprinkler module, and power module, and also equipped with a speed measurement code disk. C code written by Arduino IDE software is used to control the car, so as to realize tracking cruise and infrared obstacle avoidance functions. The car system can cruise according to the black route set in advance on the flower base, and control the car through the C code written by Arduino IDE software, so as to realize the tracking cruise and infrared obstacle avoidance functions. This design realizes the self-walking water spraying function on this theoretical basis.*

## I. INTRODUCTION

Traditional agriculture used to require a lot of manpower to solve the problem of growing crops, and today, productivity and science and technology have made greater progress, and now the young people who are willing to engage in agricultural work are decreasing, so a large number of machines is needed to replace human labor in agricultural mechanization production. In the current social environment of rapid development of science and technology, the development of science and technology has provided an innovation rate of more than 50% for the progress of agricultural science and technology. Agricultural scientific and technological innovation has been significantly improved, and the transformation and promotion of achievements have been continuously expanded and strengthened, which basically covers the production and planting of major improved crop varieties, and the proportion of livestock and poultry of excellent varieties has increased year by year. These measures undoubtedly make important contributions to ensuring the safety of food production, the effective supply of agricultural products, and the improvement of farmers'

income [1]. Agricultural science and technology is gradually becoming the core competitiveness of modern agriculture, the source of endogenous after-effects, and a new sector of transformation and upgrading. The importance of modern science and technology in agriculture is becoming increasingly prominent. The overall management level of traditional agricultural science and technology enterprises has been continuously optimized and improved, and breakthroughs have been made in basic research and strategic high-tech innovation, A large number of major innovative teaching achievements have been achieved at the world's advanced cultural level, and high-quality results have been obtained. The flower industry is one of the fastest growing and most stable industries in the world [2] and one of the sunrise industries with the greatest development potential in the world. Countries all over the world now attach importance to the development of flowers to increase their competitiveness in the international market. Efforts to develop the flower industry can occupy a favorable position in the future international competitiveness.

Science and technology are the primary productive forces. In order to enhance the competitiveness of the flower industry, it is necessary to improve the technical content of flower products [3]. In mountainous and semi-hilly areas, faced with a small area of arable land, it has brought great difficulties to mechanized operation, and mechanized planting cannot be carried out to improve efficiency and yield. Such a growing environment, if not adjusted, cannot keep up with the development of modernization and can not further improve the income of farmers.

Due to the backward development level of planting information technology and mechanization, the quality of flowers is poor and the lack of market competitiveness. At present, the sales market of high-end flowers in China mainly relies on imports, which is one of the reasons why flower products cannot be promoted quickly. In small flower planting and flower wholesale bases, flower irrigation has become a technical problem. According to the traditional artificial intelligence irrigation management method, workers need to use hand watering cans to sprinkle water, and there is a serious waste of water resources through artificial irrigation. The flower industry is labor-intensive and requires a large number of people [4]. Market feedback, general small flower plants, and flower wholesale base available labor shortage. There may be a shortage of manpower in the booming season, which leads to some flowers withering. Flower quality decline caused dehydration, to a certain extent, affecting the sales of flowers.

Under the environment of vigorously supporting agricultural innovation, with the continuous development and innovation of single-chip microcomputers technology, single-chip microcomputers has become simple and easy to learn, and the application field of single-chip microcomputer has gradually broadened, and is favored by many agricultural technical personnel. Intelligent cars based on Arduino motherboard control have also become a hot issue in the field of artificial intelligence technology. From the current market prospect analysis, self-propelled vehicles are widely used in industry, national defense, logistics, agriculture, and other fields. From the perspective of market development economic research, this design designs a self-propelled sprinkler car that should be used in small flower beds and small flower factories. The small car system can cruise according to the black route set in advance on the flower base, and it also has an infrared obstacle avoidance function. On the basis of this theory, the self-walking sprinkler function can be realized. Because the intelligent car controlled by the Arduino motherboard has a relatively complete measurement system and man-machine operating system.

Compared with other chips, it is easier to use in agriculture. Dual-function address segment of on-chip RAM, so that the user is very convenient to use, and the fault tolerance rate is low, more human. The use of multiplication and division instruction, this instruction to programming also brings a lot of convenience. Otherwise, in the case of many 8-bit microcontrollers without multiplication functions, it is very inconvenient to program and call the subroutine when multiplying. The microcontroller has been effectively developed in the development of electronic information technology. The enterprise can ensure that the microcontroller can work normally and orderly in a very complex computer and control working environment.

In order to continuously improve agricultural innovation and mechanization of flower planting in mountainous and semi-hilly areas, an intelligent self-walking sprinkler car with Arduino UNOR3 as the control board is designed in this paper. The vehicle is equipped with an ATmega328P monolithic machine, sensor expansion board, L298N motor drive module, infrared tracking sensor, infrared obstacle avoidance sensor, sprinkler module, power module, and other modules, and equipped with a speed measurement code disk. C code written by Arduino IDE software is used to control the car, so as to realize tracking cruise and infrared obstacle avoidance functions. The intelligent self-propelled sprinkler car solves the problem of serious waste of water resources caused by workers' need to carry the water bottle to sprinkle water, and also improves the mechanical rate of flower planting.

## II. HARDWARE AND SYSTEM DESIGN

### 2.1 Motor drive system

Based on the use of two 18650 lithium batteries, the L298N DC motor drive module is used to control the movement of the motor. L298N is a special drive integrated circuit, belonging to the H-bridge integrated circuit, its output current increases, power increases. Its output current is 2A, the maximum current is 4A, and the maximum operating voltage is 50V [5]. The L298N chip can drive two two-phase motors or one four-phase motor with simple circuit and convenient use, and realize the forward and reverse of the motor through the control of the I/O port [6]. Since the digital signal output of the drive module needs to be controlled to control the car, the module is connected to the Arduino UNOR3 controller. The received digital signal is processed, then fed back to the motor drive module, and finally the motor is driven to operate [7]. In the selection of the motor, because the power supply is not an AC power supply, four DC motors

are selected as the drive motor. The electric pulse generated by the DC motor during operation has less influence on the MCU, so the error can be controlled in a reasonable range. If AC motors are used, not only should the power supply be replaced with a AC power supply, but we also need to increase the AC voltage regulator. Because the DC motor can provide enough power and torque for the normal drive of the car, if the output power of the DC motor is not enough, it can also increase the torque by improving the structure of the motor wheel, so that although the speed of the car is reduced, it can provide enough power for the car to drive in the mountainous and semi-hilly areas. The specific method of motor logic forward and reverse rotation is shown in Table 1:

Table 1: Motor logic control [8]

1	IN2	ENA	Motor state
X	X	0	Stop
0	0	1	Stop
1	1	1	Stop
1	0	1	Forward
0	1	1	Reversal

## 2.2 Control module

The control board uses the ATmega328P microcontroller with 32KB memory and the ATmega16 data processing chip with 32KB memory. There are 14 digit ports on the control motherboard, six of which are PWM outputs [9]. It is also equipped with an OREF standby port for use by external extenders. Processing control chip and data processing chip, the motherboard is also equipped with a power connector to provide +5V for VCC use. The analog input interface on the motherboard can be seamlessly used with many types of digital-to-analog converters and analog-to-digital converters, so the Arduino motherboard can be perfectly combined with the sensor expansion board, with low fault tolerance, high efficiency, easy control, and accurate input and output. The USB data transmission port on the motherboard can be directly connected with the COM driver port of the computer, which reduces the error in the process of program burning. The advantage of the Arduino UNO R3 motherboard compared with the traditional STC51 microcontroller is that the motherboard is equipped with the ATmega328P microcontroller with convenient control and the ATMEGA16U2-MU(R) data processing chip with strong data processing capacity. In this way, you do not need to build a single-chip microcomputer minimum system like a 51 microcontroller to realize the processing of the electrical signal collected by the sensor. The

Arduino UNO R3 motherboard control system is simple. The built-in digital-to-analog converter and analog-to-digital converter not only make the system simple, but also make the data processing more accurate and efficient [10]. Although the circuit diagram of the STC51 microcontroller is simple, excluding the chip itself, it is necessary to attach a lot of control components to build a complete system, and the Arduino UNOR3 motherboard itself is equipped with many control components and converters, which is equivalent to the smallest system of a microcontroller.

## 2.3 Selection of single chip microcomputer

SCM has many characteristics, such as small size, high integration, easy system expansion, high reliability, and a short application development cycle [9]. According to the sensor and function requirements of the self-propelled car, the design chooses ATMEGA16U2-MU(R) as the CMOS control chip. ATmega16L, an 8-bit AVR microprocessor with high performance and low power consumption, is adopted, which can execute 131 instructions [12], which is the optimal choice of this design. Moreover, 32 programmable IO ports can be used simultaneously in the execution time of instructions in a single clock cycle. The running time of the program is greatly shortened [13]. The ATmega16 package pin definition is shown in Fig 1 :

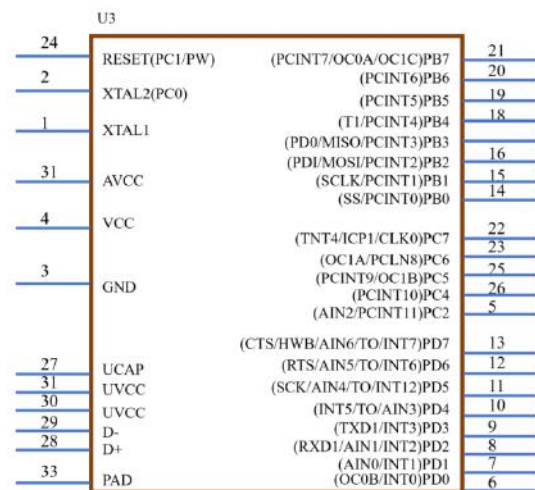


Fig 1. The ATmega16 package pin definition

Table 2. Other pin details [13]

Definition Pin	Function	Special Function
VCC	5V Power source	NC
GAD	Ground connection	NC
PAD-PA7	8-bit bidirectional I/O port	NC
PBD-PD7	8-bit bidirectional I/O port	NC
PCD-PC7	8-bit bidirectional I/O port	Timing oscillation pin
PDO-PD7	8-bit bidirectional I/O port	Input and output matching pins
RESET	Reset the output pin	NC
XTAL1	Reverse oscillation amplifies output	On-chip current is fed into the end
XTAL2	Reverse oscillation amplifies output	NC

The VCC pin in the figure is A digital power pin, GND is a ground pin, and pin PA7-PA0 is the analog input of an A/D converter. Under normal circumstances, PA is in a high resistance state, and the corresponding level of the MCU is low. Pin PB0-PB7 is also an eight-bit bidirectional I/O port, with pin characteristics similar to PA7-PA0. PC0-PC7 is also an 8-bit bidirectional I/O port, which can be connected to a pull resistor to maintain the low level of the pin [13]. The pull-up resistance can be activated if some pins are grounded and acts as a control element. At the same time, the pin PC can also be used for different special functions. Other pin details are shown in Table 2. It is precisely because ATmega16 has these advantages, so that the car can be active development in future development, but also to allow developers to achieve in-machine rectification, without destroying the integrated PCB board, you can directly carry out active development.

#### 2.4 Motor drive module

Because the DC motor has the characteristics of small size, light weight, large torque transmission, and easy control, the self-propelled sprinkler uses four small DC motors, which are installed on both sides of the chassis, to drive the four wheels of the car, which is the power part of the car. Because the output voltage of the pin is weak

through the single-chip microcomputer system at a high voltage, it is difficult to directly invest in driving the DC motor, so the L298N motor drive is installed, the software control of the L298N is simple, compatible programming languages and syntax are more, and the working voltage can reach 46V. The output current is large, the instantaneous peak current can reach 3A, and the continuous working current is 2A [5]. Rated power: 25W. The L298N chip contains two H-bridge high-voltage and high-current full-bridge drivers, which can be used to drive DC motors, stepper motors, relay coils, and other inductive loads. The external detection resistance can be connected to feed back the change to the control circuit dynamic module [15]. This design uses 4 pins provided by the module to enter the microcontroller signal, adopts a jumper cover for flexible selection, adopts PWM speed control, and bit microcontroller output pins to provide sufficient driving force for the car to run in mountainous and semi-hilly areas. The schematic diagram of the L298N circuit is shown in Fig 2.

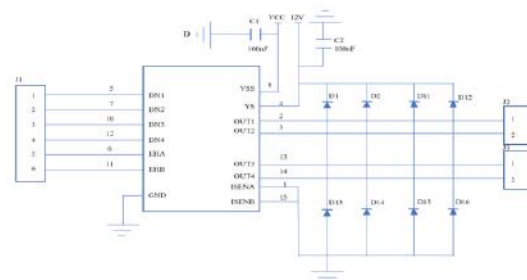


Fig 2. Schematic diagram of motor drive circuit

#### 2.5 Infrared tracking module

The infrared detection sensor module is made according to the principle that the infrared tube detects the reflected light outside the red, the deep color is weak, and the light color is strong. In the tracking process of the car to the black line, if the black line is detected, the microcontroller will return a low level. When the microcontroller pulls the level high, that is, the high level, the car stops moving forward. The distance between the front end of the photoelectric sensor and the reflector should be kept within the specified range. The sensor must be installed in a place that is not directly exposed to strong light, because the infrared light in the strong light will affect the normal operation of the infrared transmitter current of the photoelectric sensor of the receiving tube, which will reduce the anti-interference performance of the transmitter sensor on the one hand, and the sensitivity of the receiver will be stricter because the signal is too weak. The circuit schematic diagram based on TCR5000 infrared tracking is shown in Fig 3.

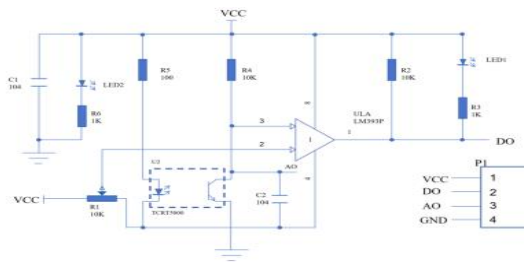


Fig 3. Circuit diagram of infrared tracking module

## 2.6 Sprinkler system

The design scheme of the sprinkler system designed in this study is to add a separate rotating nozzle to the top of the car connected to the water pipe, and the water pressure is different from the spraying range. The nozzle has two modes, adjustable Angles of 15-45 degrees, to achieve direct and oblique injection modes. Each group has four nozzles at different angles. The single-chip machine is used to drive the pulse signal of the stepper motor to subdivide the angular displacement, so that two sprinkler modes are switched by rotating the nozzle angle: direct spray for a large quantity of water, and oblique spray for a large area of water [15]. At the same time, each sprinkler rod of the three-way propeller has its own four development angles to carry out different water outlets, and each water outlet is sprayed to each corner at a different angle to make irrigation more uniform and cover a greater impact on the area. A water storage tank is installed behind the car, and then a variable flow centrifugal pump is installed, and then connected to the nozzle, so that agricultural irrigation can be achieved. The addition of water tanks and centrifugal pumps also increased the weight of the car, so it was necessary to convert two lithium batteries into storage pools to improve the durability of the car. Since the L298N can only input a maximum voltage of 33V, it is necessary to add a voltage regulator control module. This design scheme requires the car to have good waterproof performance, so the Arduino motherboard needs to be waterproof packaging. The intelligent sprinkler car can solve the problem of needing manpower to irrigate the flower field, reduce the use of labor, and improve the productivity of flowers and other.

## 2.7 Infrared obstacle avoidance module

Compared with some other infrared obstacle avoidance sensors, this design adopts the LM393 infrared obstacle avoidance module. The infrared obstacle avoidance module can be directly connected with the MCU system, and the module has its own analog-to-digital converter, so it does not need to build an analog control circuit. The working principle of infrared obstacle avoidance and infrared tracking is the same. All functions

are performed according to the degree of infrared light acceptance. Therefore, infrared obstacle avoidance is also the same as infrared tracking, which is limited by more factors and prone to problems, so other obstacle avoidance modules are needed to supplement the obstacle avoidance system of the car. The circuit of the LM393 infrared obstacle avoidance module is shown in Fig 4.

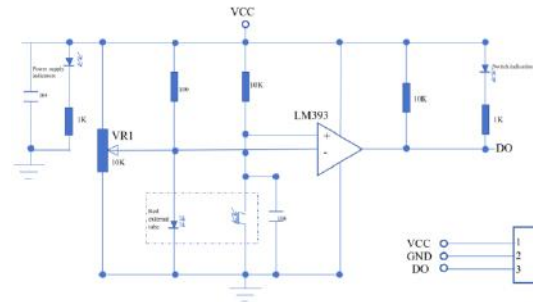


Fig 4. Circuit diagram of LM393 infrared obstacle avoidance module

In the entire control logic, the control logic of infrared obstacle avoidance and infrared tracking is the same, and even the entire control program is the same, but the definition and scope of variables are not the same.

## 2.8 Ultrasonic obstacle avoidance sensor module

Ultrasonic sensor is a range sensor. Developed according to the characteristics of ultrasonic waves, it has the characteristics of high quality and low price. Acoustic ranging refers to the use of the speed of ultrasonic propagation in the medium, by measuring the ultrasonic propagation time, calculate the distance between the measured object and the ranging equipment. The formula for the propagation speed of ultrasonic wave in the medium is:  $c = f \lambda$  [16], where  $c$  is the propagation speed of ultrasonic wave in the medium,  $f$  is the frequency of ultrasonic wave,  $\lambda$  is the wavelength of ultrasonic wave in the medium. Test distance  $D = (T \times C) / 2$ , high electric level time  $T$ , and sound speed are expressed by  $C$ ,  $C = 340\text{m/s}$  [17]. Ultrasonic obstacle avoidance is real-time and effective, which is not possessed by red obstacle avoidance. However, there are also certain limitations, such as detection time blind area, ultrasonic transmission speed instability, reverberation signal interference, and other problems [8], so this design also adds a radar obstacle avoidance sensor.

## 2.9 Radar obstacle avoidance sensor

Lidar is composed of a rotating triangle rangefinder. Through continuous rotation, measurement of the distance can be obtained with the radar as the center of the circle, the distance of a number of points around, if the data is drawn in the polar coordinate system, you can see a two-

dimensional map, if the computer has obtained a map of the space, so that the positioning of the machine is possible. This is the promising application of SLAM, also known as CML. This design intends to use ROLIDARA 1360°5.5 Hz OPTMAG optical magnetic fusion laser scanning ranging radar. The radar has a measuring range of 12 meters radius, 360 degree scanning ranging, and 8000 measurement frequencies per second. But considering the practicability problem, this design only carries on the software control to the radar module. From the analysis of software control debugging results, radar detection and control are very difficult, and the control program is larger than other sensor modules, but the core of the whole radar detection and control is not the collocation of hardware circuits but the writing of the software control program. The combination of a radar obstacle avoidance sensor, infrared obstacle avoidance, and ultrasonic obstacle avoidance improves the obstacle avoidance of the car in the process of irrigation of flowers more accurately.

### 2.10 Bluetooth remote control module

The Bluetooth module used in this design adopts the BC417143 Bluetooth chip, which is a new module suitable for wireless transmission of embedded serial ports. It not only realizes wireless communication between measurement and control instrument and PC but also wireless communication between multiple measurement and control devices and can reduce complex onsite connections [19]. The Bluetooth chip works at 3.3V, while the MCU works at 5V, and there is a logic level mismatch problem. And the T0 pin cannot tolerate the MCU's 5V logic level. For this reason, the 1117 chip is used for level conversion and 3.3V output [5]. There is much research on the influencing factors of limited control activities on PC. Many flower planting and production bases and flower wholesale bases in China are not equipped with PC terminals, which brings a lot of inconvenience to users [20]. When the flower field is not suitable for infrared tracking, the car can also be flexibly controlled by the blue tooth remote control to water the flowers.

## III. PROTOTYPE TESTING

According to the working principle of each module, the car is installed, and the C code written by ArduinoIDE software is compiled, verified, and recorded on the motherboard, and the infrared obstacle avoidance and infrared tracking functions of the car are tested. After testing and improvement, the vehicle can be used to achieve tracking cruise and infrared obstacle avoidance. After the car is fixed, the various sensors of the car are tested according to the set procedure to determine whether the car can display a specific function. Within a certain

range, draw a thick black line to test the tracking function of the car, and then test the obstacle avoidance function of the car with a straight line program. Place the car within a specific obstacle range, make the car move towards the obstacle, and observe whether the car avoids the obstacle [9]. Before the test, the ATmega16 chip and ATmega328P chip need to be tested. Only when these two chips work properly, can the subsequent test be carried out normally. It is difficult to test ATmega16 directly, so the 51 MCU learning board is used for auxiliary testing. In this test process, an AD converter and a DA converter are required. During the process of screwing the potentiometer, if the digital tube on the test board can respond to the corresponding change and the digital tube shows a value between zero and two hundred and fifty-five, it is normal [20]. In order to make the test results more accurate, two test programs are used to test, one is to respond to the change of AD, and the other is to respond to the change of DA. After the test, it was found that the display of the digital tube was normal, and then the DA was tested, and this test process only needed to observe the process of the LED going from dark to light and then out. After testing, it was found that the LED appeared from dark to light and then to extinguish the phenomenon, which is a normal phenomenon.

According to the above test results, the ATmega16 chip can process data normally and act as a data processing chip, which meets the design requirements [13]. After testing the ATmega16, the ATmega328P chip is also required to be tested to ensure the normal operation of the self-propelled car. This test is based on the 51 microcontroller learning board. During the test, the 80C51 microcontroller on the learning board is replaced by the ATmega328P microcontroller. Because the temperature signal is the easiest signal to detect and process, this design uses temperature as a variable to test the response of the L298N drive motor based on ATmega328P control. Set at a certain temperature, when the temperature is greater than or equal to the temperature, the motor runs, when the temperature is less than the temperature, the motor stops running. In order to observe the temperature change more clearly, it is necessary to display the temperature on the computer through serial communication to ensure the accuracy of the test results [11]. Before using serial communication, it is necessary to test the COM port of the computer, and the next test can be carried out after the test is wrong. After the test, the working state of the LED can be accurately fed back to the computer, that is, the COM of the computer meets the serial port exchange protocol, so the next test can be carried out. After testing, the MCU can respond to the changes of the sensor, and the MCU can also control L298N according to the different values for

different actions. From the above tests, it can be seen that there is no temperature of slow response and inadequate response of the monolithic machine, and there is no problem of data processing error and unsuccessful response of the data processing chip. Therefore, the hardware circuit can be built and all modules can be tested.

#### IV. RESULTS AND DISCUSSION

Multiple rounds of repeatability experiments were carried out to consolidate the reliability of the experimental results and verify their repeatability, and the functional test results of cars numbered 1 to 15 were analyzed, as shown in Table 3. As can be seen from Table 3, no exception was found in each user module in the second, third, ninth, eleventh, fourteenth, and fifteenth tests, and no exception was found in the other tests. From the whole test results, except for the sixth experimental test, there is only one module exception in each exception test. In the sixth test, infrared sensor tracking and ultrasonic obstacle avoidance were abnormal. The number of infrared obstacle avoidance anomalies was 3, 4, 8, and 13, respectively. There are six and ten anomalies in the infrared tracking. There were 5 ultrasonic obstacle avoidance anomalies, which were 1, 5, 6, 7, and 12 times, respectively. From the frequency analysis of the fault, the frequency of some faults in ultrasonic obstacle avoidance reaches the highest, followed by infrared obstacle avoidance, and finally infrared tracking. It can be seen from the above analysis that, in addition to the motor drive, other modules have anomalies in the test process, among which the ultrasonic obstacle avoidance module has more abnormal times, and the infrared tracking and infrared obstacle avoidance module has fewer abnormal times. The L298N motor drive module is hardware controlled, so the failure rate is zero.

N: Normal

U: Unnormal

Table 3 Test experimental data

module Serial number	Infrared obstacle avoidance	Infrared tracking	Ultrasonic obstacle avoidance	Motor drive
1	N	N	U	N
2	N	N	N	N
3	N	N	N	N
4	U	N	N	N
5	N	N	U	N

6	N	U	U	N
7	N	N	U	N
8	U	N	N	N
9	N	N	N	N
10	N	U	N	N
11	N	N	N	N
12	N	N	U	N
13	U	N	N	N
14	N	N	N	N
15	N	N	N	N

When the infrared tracking module works, infrared rays are emitted from the TCRT5000 sensor. If the emitted infrared rays are not reflected back by the ground or have been reflected back, in this case, the voltage of pin 3 is lower than the voltage of pin 2, the DO of the output pin is high, and LED1 is in the off state. Otherwise, the sensor has the following characteristics: the detection reflection distance is 1mm-25mm; LM393 output, strong driving capacity, more than 15mA; operating voltage: 3.3V-5V [11]; TCRT5000 infrared reflection sensor is adopted. Due to the limited detection reflection distance, a length of 5 mm should be reserved when installing the infrared tracking sensor. In the process of testing, the front end of the sensor should be parallel to the work piece object to be tested, so that the conversion efficiency of the photoelectric sensor is the highest. The distance between the front end of the photoelectric sensor and the reflector should be kept within the specified range. The sensor must be installed in a place where it is not directly exposed to strong light, because the infrared light in the strong light will affect the normal work of the current of the infrared transmitter of the photoelectric sensor of the receiving tube, which will reduce the anti-interference performance of the transmitter sensor on the one hand, and the sensitivity of the receiver will be stricter because the signal is too weak. The probability of infrared obstacle avoidance problems is higher than that of infrared tracking. Not only the light has an impact on the obstacle avoidance sensor, but as long as the time is long, the impact of the LED emission line frequency on the obstacle avoidance function of the entire car is also self-evident.

Compared with infrared obstacle avoidance, although the range of distance measurement is not very large, the accuracy of the ultrasonic ranging system can reach the upper level of millimeters. Using a serial debugging assistant and an oscilloscope to assist the test, the realization of the system is more reliable. Of course, there are many factors that affect ultrasonic distance

measurement, but as long as the program control is done well, the advantages of ultrasonic obstacle avoidance are far greater than infrared obstacle avoidance. Infrared tracking, infrared obstacle avoidance, and ultrasonic obstacle avoidance are controlled by software, with more shadow and noise factors and a higher failure rate than motor drive modules. In software control, the key factor is the program itself, the code quality directly affects the stability and reliability of the system. By optimizing code structure, simplifying logic, and adopting good programming habits, the probability of program error can be significantly reduced, and the maintainability and extensibility of the system can be improved. Therefore, it is necessary to optimize the design of C code, improve variables, syntax, and parameters, and use two designs to represent certain statements in the program, the alternate control program. Because of the compatibility problem of the control program, the backup program can play a protective role in the process of software debugging. At the same time, the standby program as a comment does not take up chip memory. In Bluetooth control, by simplifying C code, the problems of Bluetooth module matching failure, data transmission being inaccurate and not timely are solved.

(1) C code before modification

```
Void blinker_car_detect(){if (!digital
Read(C_BAR_PIN))
{if (!is Warn){
Blinker.vibrate();Is
Warn=true;car_os_time=millis();}
Else if (millis()-car_os_time>=5000)
{isWarn=false;}}
else{
Is Warn=false;}}
```

Modified C code:

```
Void
bilnker_car_control(uint8_tcl_pwm,boolcl_dir,uint
8_tcr_pwm,boolcr_dir)
{digitalWrite(IN4,cl_dir);DigitalWrite(IN1,cr_dir);
Analog Write(IN3,cl_pwm);Analog
Write(IN2,cr_pwm);}
```

(2) C code before modification:

```
#if defined(BLINKER_CAR_DEBUG)
BLINKER_LOG4("L_PWM:",L_PWM,"|L_DIR:",
L_DIR);//Return value
BLINKER_LOG4("R_PWM:",R_PWM,"|R_DIR:"
,R_DIR);Blinker.delay(2000);
```

#end if

Modified C code:

```
{void loop()
Blinker.run();{if ((millis()-t)>timeout)//Read the
number value directly without returning it
t=millis();timeout=2000;blinker_car_init();}
```

The modified code uses complex embedded syntax, which is easy to cause numerical reading errors, while the modified code uses function parameters to reduce embedded statements to pass the PWM value and direction of the left and right wheel, avoiding the use of global variables, making the function more modular and easy to maintain, and making the code numerical reading more accurate. It can be seen from before and after the modification that the modified code is simpler and the syntax is clearer. By simplifying logic, standardizing variable naming, and adopting function encapsulation, the readability and maintainability of the code are improved, and the error probability is reduced. It not only reduces the size of the entire program, but also significantly the probability of program errors. The application of Bluetooth modules in intelligent cars is increasingly widespread, but its real-time and stability still need to be further improved. By optimizing the Bluetooth communication protocol and data processing algorithm, the accuracy and timeliness of data transmission can be improved to meet the needs of more application scenarios. In summary, the intelligent sprinkler car based on a single chip microcomputer has achieved remarkable results in ultrasonic ranging, C code optimization, and Bluetooth control, which provides a useful reference for the development of the intelligent car field. In the future, the comprehensive performance and stability of the system can be improved through further technological innovation and optimization.

## V. CONCLUSION

This design is based on the control of Arduino by the motherboard to increase the sprinkling function. After the system is powered on, the designed intelligent irrigation car shows good reliability, stability, and fast response speed. The car can set the irrigation route of crops in advance according to the flower base, which solves the problem of inconvenient watering time of small flower beds and flowers to a certain extent, and the system can provide convenient watering of flowers for some people who like to cultivate flowers but have difficulty moving. It also brings convenience to flower planting and flower wholesalers to a certain extent, improves work efficiency, and also promotes the application of agricultural innovation in planting flowers. At the same time, this

design has more room for development. In addition to the conventional red obstacle avoidance and infrared tracking functions, the addition of Bluetooth control, ultrasonic obstacle avoidance, radar detection, and scanning functions will make the car in mountainous and semi-hilly areas more flexible to avoid obstacles and more safe driving.

### ACKNOWLEDGEMENTS

The work described in this paper was supported by the 2024 College Student Innovation and Entrepreneurship Competition of Guangdong University of Petrochemical Technology, "Air Conditioning Pipe Cleaning Based on 51 Microcontrollers" under Grant No: 710135124189.

### REFERENCES

- [1] Yang L. P. (2012). Brief introduction of flower industry. Science and Technology Training for farmers (03), 23-24.
- [2] Lin Jianzhong, Lai Ruiyun, Li Jinyu & Lai Zhongxiong. (2008). World flower industry development overview. Journal of Minxi Vocational and Technical College (02), 80-84.
- [3] Ran Cai hong.(2015). The present situation of Chinese flower industry and the countermeasures to enhance competitiveness. Southeast reduces Horticulture (01), 36-38.
- [4] Zhang N. (2014). Research on the development trend of Floriculture Industry in China and the Status quo of Floriculture industry in Key producing areas of Shandong Province (Master Dissertation, Shandong Agricultural University).
- [5] Liu XR, Guo ZQ & Feng Fei, (2016). Multi-function remote control small car design. Science and Technology Outlook (23), 180.
- [6] Chen Zhibin & Lin Shouying. (2020). A brief analysis of the design points of remote control sprinkler car based on 51 single chip microcomputer. Southern agriculture (33), 191-192.
- [7] Zhang Junwei. (2020). Design of experimental device of rotary inverted pendulum based on stepper motor. Science and technology (29), 14-15.
- [8] Jun-tao wang, He Chuan, Yao Jianyun & YanYiMin. (2013). Light control automatic curtain rail design. Experimental Science and Technology (03), 184-187.
- [9] Zhao Guangping. (2023). Design of intelligent tracking and obstacle avoidance car based on single chip computer. Paper Equipment and Materials (03), 13-16.
- [10] Li Qi.(2015). Master of Smart Home System Design based on Android Platform (Dissertation, Hangzhou Dianzi University). Master
- [11] Sun Yuwei, Wang Huaixia, Shi Yan & Zheng Qijia.(2020). Intelligent control device of feeding box based on single chip machine. Electronic Technology and Software Engineering (15), 104-105.
- [12] Chen X. (2016). Master of Mobile Robot Platform and Online Monitoring System Design and implementation (dissertation, Zhengzhou University). Master
- [13] Wei Jinling.(2020). Design of intelligent clothes drying system based on MCU control. Electronic world (23), 113-115.
- [14] Bai Zhiqing. (2020). Design of micro-liquid injection system based on microcontroller. Journal of jiangnan university (natural science edition) (02), 54-58.
- [15] Qiu Gang.(2007). Development of on-line monitoring device for Ground fault of DC feeder of tram. Master's Thesis, Beijing Jiaotong University.
- [16] Shu XiuLan. (2013). Design of ultrasound ranging system based on AT89C2051 single chip computer. Digital technology and application of (6), 159 + 161.
- [17] li xinfeng port & often. (2021). Anti-collision anti-theft alarm based on 51 microcontroller ultrasonic ranging. Electronic test (19), 27-29.
- [18] Chen xin. (2016). Master of Mobile Robot Platform and Online Monitoring System Design and implementation (dissertation, Zhengzhou University).
- [19] Jin Zhen, Tang Minghao, Zhou Hualan, He Jie.(2004). Design of intelligent measurement and control system based on Bluetooth wireless interface. Journal of Donghua University (Natural Science Edition)(01), 72-75.
- [20] Ye Chunyuan, Yu Xia, Yang Yanran & Guo Jiaying.(2020). Drip detection system based on STC89C52 single chip microcomputer. Automation should be to use (7), 154-156.

# Air Conditioning Design for Comfort Impact on the Human Body in Small Vehicles

Jin-Ping Chen, Yan-Zuo Chang\*, Ruo-Yu Yang, Jian-Ting Lai, Pei-Xin Wu

Institute of Energy and Power Engineering, Guangdong University of Petrochem Technology (GDUPT), Maoming, 525000, China

\*Corresponding author: 18027600852@163.com

Received: 16 Jul 2024,

Receive in revised form: 18 Aug 2024,

Accepted: 25 Aug 2024,

Available online: 31 Aug 2024

©2024 The Author(s). Published by AI  
Publication. This is an open-access article  
under the CC BY license

(<https://creativecommons.org/licenses/by/4.0/>).

**Keywords**— Car Air Conditioning, Human  
Comfort, PMV, PPD

**Abstract**— This paper uses the theory of Heat Exchangers to estimate the relationship between the outlet and the inlet and is written in conjunction with Fluent to simulate the impact of the air conditioning system on the environment in the car. The outside environment also affects the inside of the car, and this paper experiments to obtain outlet environment data and set it as the boundary conditions. The thermal comfort index in this paper will use experimental parameters to compute the results and analyze the results of the data to address people's requirements for the quality of the driving environment and provide a better driving environment.

## I. INTRODUCTION

In vehicle design, thermal comfort not only affects the immediate feelings of passengers but is also closely linked to driving safety, health, and energy efficiency [1]. An appropriate temperature in the car reduces the driver's feeling of fatigue and increases his attention and response speed, thereby reducing the risk of traffic accidents. In addition, at comfortable temperatures, the body's physiological function is more stable and can effectively avoid physical discomfort caused by heat or overheating, such as colds, strokes, or joint pain [2]. From an energy-efficient point of view, a reasonable heat comfort design can optimize the use of the air-conditioning system, reduce unnecessary energy consumption, and have a positive impact on environmental protection and the economy.

The in-room heat comfort model is a very important technical problem in the design of an in-room heating and air conditioning system [3]. The model is composed of two parts, namely, the Model of Calculation of the Comfort of the Heat Environment in the Car and the Model for Calculating the Comfortable Heat in the Car [4]. The first one is studied by three professors, Wang Baoguo, Jin Yanmei and Liu Shuyan. This model is mainly aimed at

the problem of the thermal comfort of the human body in the car. The model uses the Calculative Model of Comfort in the Thermal Environment and the calculative model of the assessment of the caloric comfort in the body of the car under the Non-uniform Thermal Comfort Environment proposed by three professors. It can analyze and predict the heat comfort problems of the whole car room. This has an important role in improving the structure and design of the air conditioning system in the vehicle.

With the advancement and development of modern computer engineering science technology, computer technology can be used to solve fluids that meet various constancy conditions controlled by partial equation groups. The mathematical calculation of indoor flow has also made great progress and development in the technology of fluid mechanics. CFD methodology is currently a strong engineering scientific research and application field internationally and is the core and important technology for air conditioning systems to conduct "three transmissions": heat transmission, transmission of motion and indoor air combustion, multi-phase flow, and chemical reaction engineering research [5].

Using the fluid mechanics CFD method, we can simulate and predict the phenomena of the speed field, temperature field, humidity field, and hazardous concentration fields of indoor air flow. This not only achieves the overall performance of the air conditioning system that can be simulated and forecast indoors, but also the possibility of multiple virtual product developments in the interior, which greatly reduces the number of actual trials, the cost of trials, and the shortening of trial cycles.

Therefore, using the CFD model and FLUENT simulation, numerical simulation experiments can be performed faster and faster. The known in-car environment analysis is closely related to the impact of the air-conditioning system in the car and the outside environment. For the in-vehicle air conditioning system, the theory of Heat Exchangers is used in this paper to estimate the relationship between the outlet and the back outlet of the car [6]. For an outside environment, this paper uses the values obtained from the real car experiment as the boundary conditions. In addition, consider the  $k-\epsilon$  mode and the heat transmission of the cabin. The above conditions are introduced into the FLUENT simulation software to obtain changes in the temperature field and the speed field of the vehicle, and the results are predicted by the thermal comfort index PMV forecast method to predict the passenger's heat comfort and build a set of heat comfort software to analyze the comfort of the environment inside the car.

With the model of the bridge car containing air conditioning, this study is mainly divided into the following four aspects for improving the problem of human heat comfort in cars: (1) Based on the theory of fluid fluid viscosity, the RNG  $k-\epsilon$  fluid model has been used to calculate the air flow and temperature distribution in the car room. (2) In order to reflect as much as possible the authenticity of the physical model, the effects of various heat loads on the in-vehicle flow fields were taken into account in the establishment of the mathematical model, and the biological thermal boundaries were considered. (3) the construction of a common car physics model with the appropriate simplification of the area of study in order to study the effect of solid regions on the distribution of air flow speed in the vehicle room. (4) use FLUENT software for numerical simulation of the air conditioning car room; study to analyze the change in the air flow field in the car room when different ventilation positions and ventilation parameters are used; compare the various air flow organizations; and provide a reference for optimization of design.

## II. EFFECTS OF HEAT LOADS ON HUMAN COMFORT

The energy balance equation of the human body and its surroundings is based on the energy equilibrium equation developed in the ASHRAE Handbook of Fundamentals [7] :

$$M - W = Q_{sk} + Q_{res} + S = (C + R + E_{sk}) + (C_{res} + E_{res}) + S_{sk} + S_{cr} \quad (1)$$

Among these are:  $M$ -human metabolism rate, (W/m<sup>2</sup>);  $W$ -humane metabolism, (W/m<sup>2</sup>);  $Q_{sk}$ -heat loss caused by skin, (W/m<sup>2</sup>);  $Q_{res}$ -thermal loss caught by respiration, (W/m<sup>2</sup>);  $S$ -heating energy stored by the human body, (W/m<sup>2</sup>);  $C$ -heater loss cause of fluid in the skin, (W/m<sup>2</sup>);  $R$ -heather loss cause of radiation in skin, (W/m<sup>2</sup>);  $C_{res}$ -Heat Loss from Respiration, (W/m<sup>2</sup>);  $E_{sk}$ -Heat loss due to evaporation from skin, (W/m<sup>2</sup>);  $E_{res}$ -Heating loss caused by evaporating breathing, (W/m<sup>2</sup>);  $S_{sk}$ -Heat storage from skin, (W/m<sup>2</sup>);  $S_{cr}$ -Heating storage in the body, (W/m<sup>2</sup>).

In general, the body temperature is maintained at approximately 37 °C [8], and when the temperature of the body falls below the external ambient temperature, it is controlled by some mechanisms to maintain the temperature. The body's temperature adjustment system, based on equation (1), controls the temperature at a constant temperature, avoiding too high or too low temperatures.

When the body temperature is too high to reduce the heat loss rate, the blood vessels shrink and change the blood flow rate. The heart also slows down its beat rate, and with the evaporation of sweat, the temperature decreases [10]. On the contrary, when the body's temperature is so low, the body produces unself-sufficient muscle tremors to increase heat loss, resulting in a rise in body temperature.

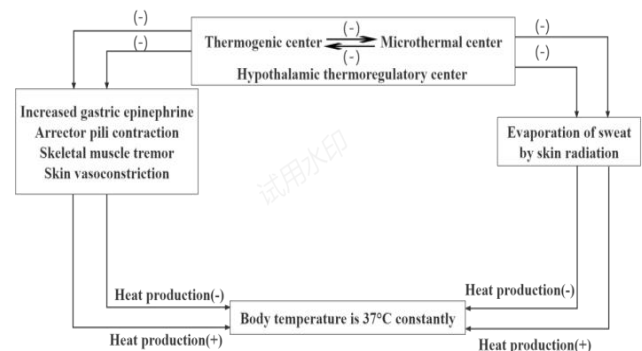


Fig.1: Human thermal balance ratio chart (representing- decrease, +increase)

**2.1 PMV indicators**

The most common and widely used indicators for assessing thermal comfort are *PMV* (predicting average voting) and *PPD* (predictive dissatisfaction percentage). The *PMV* indicator is used to measure the comfort of a person in an environment [10], generated by a subjective assessment by many subjects of certain environmental conditions in a particular environment. In order to take into account the differences among different individuals, the *PPD* indicator has been developed in the form of percentages to represent the proportion of individuals who will feel dissatisfied under the same conditions.

The *PMV* indicator is proposed by *Fanger* [10–11], controlled by the six parameters of air temperature, relative humidity, average heat radiation temperature, clothing thermal insulation value, degree of human activity, and relative air flow rate. The theoretical formula is:

$$PMV = (0.303 \cdot e^{-0.036M} + 0.028) \times [(M - W) - H - E_c - C_{res} - E_{res}] \quad (2)$$

Among them : *M*-human metabolic rate; *W*-acquired power; *H*-human body dry heat loss rate; *C<sub>res</sub>*-human respiratory thermal convergence exchange law; *E<sub>c</sub>*-the evaporative heat exchange rate of the human body at the heaviest heat sensing state; *E<sub>res</sub>*-the human respiratory evaporation thermal conversion rate.

This theoretical formula (2) has been developed continuously and has been formulated by the ISO-7730 standard as follows:

$$PMV = (0.303 \cdot e^{-0.036M} + 0.028) \cdot \left\{ \begin{array}{l} (M - W) - 3.05 \times 10^{-3} \cdot [5733 - 6.99 \cdot (M - W) - p_a] \\ - 0.42[(M - W) - 58.15] - 1.7 \times 10^{-5} \cdot M \cdot (5867 - p_a) \\ - 0.0014 \cdot M \cdot (34 - t_a) - 3.96 \times 10^{-8} \cdot f_{cl} \cdot \left[ \frac{(t_{cl} + 273)^4}{(t_r + 273)^4} - 1 \right] \\ - f_{cl} \cdot h_c \cdot (t_{cl} - t_a) \end{array} \right\} \quad (3)$$

$$t_{cl} = 35.7 - 0.028 \cdot (M - W) - I_{cl} \cdot \left\{ \begin{array}{l} 3.96 \times 10^{-8} \cdot f_{cl} \cdot \left[ \frac{(t_{cl} + 273)^4}{(t_r + 273)^4} - 1 \right] \\ + f_{cl} \cdot h_c \cdot (t_{cl} - t_a) \end{array} \right\} \quad (4)$$

$$h_{cl} = \begin{cases} 2.38 \cdot (t_{cl} - t_a)^{0.25} & \text{for } 2.38 \cdot (t_{cl} - t_a)^{0.25} > 12.1 \sqrt{V_{ar}} \\ 12.1 \sqrt{V_{ar}} & \text{for } 2.38 \cdot (t_{cl} - t_a)^{0.25} > 12.1 \sqrt{V_{ar}} \end{cases} \quad (5)$$

$$f_{cl} = \begin{cases} 1.00 + 1.290 \cdot I_{cl} & \text{for } I_{cl} < 0.078 m^2 C / W \\ 1.05 + 0.645 \cdot I_{cl} & \text{for } I_{cl} < 0.078 m^2 C / W \end{cases} \quad (6)$$

Among these, *M*-human metabolic rate ( $W/m^2$ ) ; *W*-external work ( $W/m^2$ ) ; *t<sub>a</sub>*-air temperature ( $^{\circ}C$ ) ; *I<sub>cl</sub>*(=*clo*) -clothing thermal insulation val ( $0.155 m^2 C/M$ ) ; *h<sub>c</sub>*-heat-transmission coefficient ( $W/m^2 C$ ) ; *t<sub>cl</sub>*-clothing surface temperature ( $^{\circ}C$ ) ; *f<sub>cl</sub>*- ratio of the area covered by clothing to the area not covered; *V<sub>ar</sub>*-relative air flow rate (m/s) ; *P<sub>a</sub>*-partial vapour pressure (pa) ; *t<sub>r</sub>*-average radiation temperature ( $^{\circ}C$ ) .

The *PMV* index is the average value of the estimated group of 7 levels of heat sensation based on human thermal balance (see table 2). When the heat generated in the body is equal to the heat dissipated into the environment, the person is in thermal equilibrium. In medium environments, the body's thermal adjustment system automatically adjusts the temperature of the skin and the amount of sweat to maintain the heat balance.

According to the ASHRAE comfort scale, the *PMV* value is divided into seven, from +3 to -3. When the calculated *PMV* value is zero, it indicates that the human body feels most comfortable in this state; +3 and -3, respectively, indicate that the person feels extremely hot and extremely cold in this condition.

Table 2: Seven levels of sensation measurements

PWV	Thermal sensation
+3	Hot
+2	Warm
+1	A little warmer
0	Moderate
-1	A little cool
-2	Cool
-3	Cold

**2.2 PDD indicators**

The *PMV* indicator is a subjective indicator that, in order to take into account individual differences, derives the *PPD* indicator, which is used to estimate the degree of human dissatisfaction with the environment [10]. When the *PMV* indicator is sought, the following relationship formula can be used to solve the *PPD* indicator:

$$PPD = 100 - 95 \cdot \exp \left[ - \left( 0.03353 PMV^4 + 0.2179 PMV^2 \right) \right] \quad (7)$$

When the *PPD* indicator is between +5 and -5, the discomfort ratio for the general person is within 10%, so *PPD* values within this range can be identified as comfortable.

**2.3 Correspondence between PDD indicators and PMV indicators**

The *PPD* indicator is obtained based on the *PMV* indicator, and there is a correlation between it; the perpendicular axis is *PMV*, and the perverse axis is *PPD*, calculated as a percentage. When *PMV* is zero, the corresponding *PPD* index is 5%, indicating that only about 5% of people are likely to feel uncomfortable when the calculated *PMV* index is 0 when the body feels most

comfortable. We can use this relationship to make a more objective assessment of thermal comfort.

This paper uses an experimental combination of CFD analyzers to obtain the six parameters needed to calculate the *PMV* value. Bringing the six into the procedure written by equations (2) to (7), the relationship between *PMV* indicators and *PPD* indicators can be obtained, and the thermal comfort of passengers in the vehicle can be analyzed using this relationship.

### III. NUMERICAL SIMULATION OF AIR FLOW ORGANIZATION IN THE AIR CONDITIONING VEHICLE

This paper is mainly about solving the problem of human body thermal comfort in the environment, and this problem mainly lies in the adjustment of air conditioning. Ventilators are an indispensable part of air conditioning. When adjusting the temperature, the winding angle of the ventilators is also important. For this, we chose winding angles of 30 degrees, 45 degrees, and 60 degrees to discuss. In this process, we measure the frequency of fixed winding leaves.

Therefore, this paper uses Fluid to simulate the winding width of the fan leaf, leading to changes in the internal flow field of the car. Figure 3 is a numerical simulation of the process map. First, we need to establish the internal grid, then the boundary conditions, temperature, and humidity measured by the grid and the experiment measurement of the vehicle with the fluent to solve the temperature field and flow field in the vehicle, and finally, by comparing the experiment and the calculated temperature field to verify the process and predict *PMV* and *PPD*.

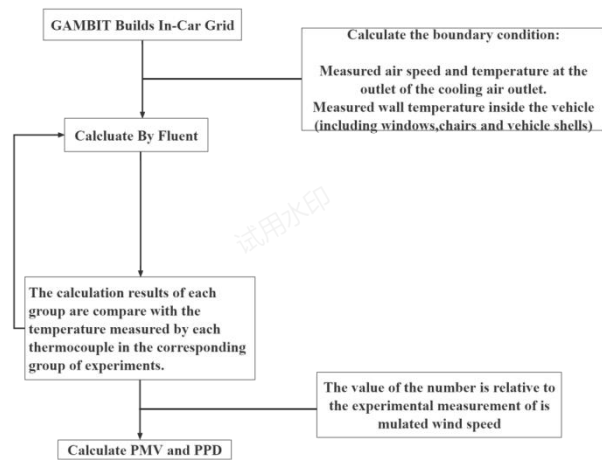


Fig.3: Fluent-Simulated Process Chart

### 3.1 Inside and outside of the vehicle

The software used by GAMBIT is the FLUENT preprocessor. GAMBIT can build a geometry (CAD), build a mesh, check the quality of the mesh, and set the boundary area. In the area of the grid, GAMPIT can create a structural and non-structural mesh. The type of mesh it provides is quadratic, five-faceted, hexadecimal, and so on.

### 3.2 Numerical methods

In Fluent, the main dominant equations sought to be solved are: continuous, dynamic, and energy equations [12]. In the mathematical model, in order to simplify the problem, Fluent uses the concept of the limited volume method to convert the dominant to the algebraic equation so that it can be resolved numerically. This limited volume approach exists for each control volume in the dominant form of a point, i.e., in a dispersed equation that holds the physical masses in the control volume. If  $\phi$  represents an arbitrary physical mass, to disperse the dominance equation, it is first to represent in a point form  $\phi$  the stable observation transmission of a controlling volume  $V$  as follows:

$$\int \rho \phi \vec{V} \cdot d\vec{A} = \int \Gamma_{\phi} \nabla \phi \cdot d\vec{A} + \int S_{\phi} d\vec{v} \quad (8)$$

Among them are:  $\vec{V}$  -velocity vector;  $\vec{A}$  -vector-oriented;  $\Gamma_{\phi}$  - $\phi$  dispersion coefficient;  $S_{\phi}$  -source flow item per  $\phi$  unit of volume;  $\rho$  -density.

The formula (13) can be applied to the control volume or grid in the computational field. In solving the problem of pressure-speed-field fusion, the SIMPLE algorithm is used to solve the problem. The SIMPLE algorithm [13] uses speed and pressure correction to force quality constancy and solve pressure fields.

### 3.3 Border conditions and convergence conditions

In terms of temperature setting, the boundary conditions of the non-stable temperature field and time change in the search engine are set to adjust the temperature of the cold air outlet measured by the experimental volume to the data of the change in time, and the corrected equation is written as a custom function hanging in FLUENT.

When the change in the stable temperature field in the car, the flow field, is to wait for the state of the car to stabilize, measure the temperature of the outlet of the cooling air, the window temperature, the interior temperature, and the seat temperature, and use the average value as the boundary conditions. In setting the wind speed of the cold air outlet, it is directly measured by measuring wind speed as the boundary condition. At the passenger's boundary conditions, the heat yield rate is 58/mw when the body is sitting, while the body temperature is set to

34.5 °C on the surface of the clothes. Table 5 provides the setting of all boundary conditions. Convergence conditions, with the residual value to make judgment procedure convergence. After the boundary conditions and convergence conditions are determined, the final output can be obtained using fluid for simulated calculations.

Fig.4: Boundary conditions set

Boundaries	Set
Cold air outlet	At the inlet (for a given amount of measured with speed and temperature)
Exhaust port	Flow at exit (free boundary condition)
Inside the hub	Vehicle surface (given measured temperature)
Chair	Vehicle surface (given measured temperature)
Passenger	Car surface (given the rate of heat generation and the body temperature measured while sitting)

The convergence criterion in this paper in the energy equation is based on  $10^6$ , and all other physical masses are based on  $10^3$ .

#### IV. AIR-CONDITIONING DESIGN

##### 4.1 Car Air Conditioning Heat Load

The condition for the calculation of the heat load of the air conditioning is that all the heat transfer area of the car is  $1.96 \text{ m}^2$  in the roof area and  $5.42 \text{ m}^2$  on the side; all heat transfer parts are based on the thickness of the cross-section of the SUV model; the speed of the vehicle is set at  $V=40 \text{ km/h}$ ; and the compressor speed is based on 3.0 L of the Hyundai SUV engine [14].

The heat load of car air conditioning is mainly the heat load from new and leaked winds, the heat dissipation of the driver and passengers in the car, the heating transmission of the body structure and the outside, the thermal load of the electronic equipment and lighting lamps in the vehicle, the engine heat transmission, and so on.

##### 4.1.1 Determination of conditions

Regarding the conditions in the vehicle, According to actual experimental data, the temperature of 24 to 26 °C is the optimal temperature that the human body feels in a hot summer, so the setting of the indoor temperature is:  $t_1 = 25 \text{ °C}$ . When the relative humidity in the cabin is less than 30% or greater than 70%, the body will feel uncomfortable,

but it will be more comfortable when it is in the range of approximately 45 to 60%. On the basis of human hygiene requirements, each person should have 16 to 33  $\text{m}^3/\text{h}$  of new wind. Taking into account the possibility that the car may be parked regularly or the passenger switched the door, the air exchange volume is set here:  $V = 55 \text{ m}^3/\text{h}$  (at 11  $\text{m}^3/\text{h}$  per person).

Regarding the outside conditions of the car, this paper takes into account the internal and external environments commonly used by the hot and high temperatures of the summer and the car air conditioning system, as well as searching for the relevant information [15], so the outer boundary conditions of this car are determined as: sunlight intensity:  $I_{level} = 0.98 \text{ kW/m}^2$ ;  $I_{vertical} = 0.16 \text{ kW/m}^2$ ;  $I_{dispersed} = 0.04 \text{ kW/M}^2$ ; ambient temperature:  $t_2 = 40\text{°C}$ ; relative humidity:  $\phi=60\%$ .

##### 4.1.2 Determination of the hourly driving speed and speed of the compressor

The timing speed of the car and the compressor is defined as: timing velocity:  $V=40\text{km/h}$ ; compressor belt wheel diameter:  $d_{pressure}=120\text{mm}$ ; engine belt wheels:  $d_{speed}=137.4\text{mm}$ ; tire rolling radius:  $r=0.319 \text{ mm}$ ; gearbox main deceleration ratio:  $i_0=3.978$ ; gearboxes 3 degrees reduction ratio:  $i_3=1.0$ ; gearbos 4 degrees deceleration ratio:  $i_4=0.72$ ; engine/compressor drive ratio,  $i=1.145$ ; compression engine rotation speed,  $N_{pressure}=1516 \text{ rpm}$ ; compressor rotation rate,  $N_{voltage}=1090 \text{ rpm}$ ; compressors average rotation:  $N_{average}=1303 \text{ rpm}$ ; counter-engine rotation,  $N_{output}=1324 \text{ rpm}$ ; and counter-generator rotation velocity,  $N=952 \text{ rpm}$ ; engine output at 1140 rpm: 20KW.

##### 4.1.3 Establishment of thermal balance relations

The heat load of the car is composed of the various heat loads that enter the cabin. The approximation of the stable heat transfer is used in the following processes as the thermal balance ratio [7-16]:

$$Q_e = Q_1 + Q_2 + Q_3 + Q_4 + Q_5 + Q_6 + Q_7 \quad (9)$$

In the formula:  $Q_e$ : air-conditioned heat load;  $Q_1$ : heat load into the cabin through the car's roof, door, and other body-covering structures;  $Q_2$ : heat load in the cabinet through the engine cabin;  $Q_3$ : heat load through the floor into the car cabin;  $Q_4$ : heat load inside the car through the door window glass and windshield;  $Q_5$ : New air winds bring the heat load to the cabins;  $Q_6$ : Heat load of the motor and lighting lamps in the car;  $Q_7$ : heat load dispersed by the human body and the heat dissipation of other objects in the vehicle.

##### 4.2 Determination of the cooling volume of the air-conditioning system

$$\text{In the formula : } Q = \alpha_1 Q_e \quad (10)$$

The  $\alpha_1$ -reserve coefficient can be picked from 1 to 1.2; the reserve factor is corrected. The value is 1.02. That is, at a speed of 40 km/h, the system cooling capacity should reach about 4611.8 W.

**4.3 Determination of refrigerant circulation flow**

The coolant cycle is the core part of a coolant system, and its basic function is to absorb and release heat through the phase change of the coolant (liquid to gas, gas to liquid), thereby achieving a cooling effect.

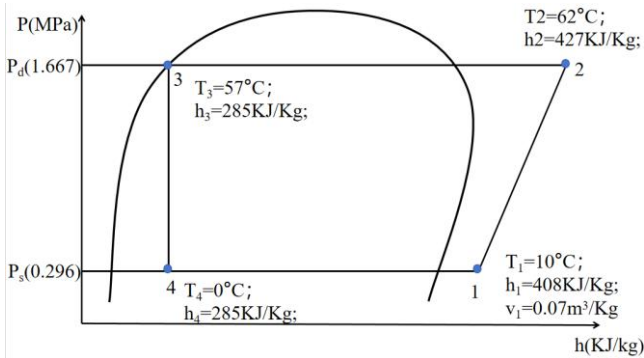


Figure 5: Working pressure chart of the air conditioning system

1 to 2 is the equilateral mercury compression process; 2 to 3 is the equilateral pressure condensation process; 3 to 4 represents the equilibrium merger flow process. 4 to 1 represents the equilibrium pressure evaporation process.

1 of these points indicates the point of inhalation of the compressor; 2 points indicate the exhaust point;  $P_d$  indicates condensation pressure;  $P_s$  indicates evaporative pressure;  $T_s$  indicates air temperature;  $T_d$  indicates the exhaust temperature;

Mass flow of refrigerant cycle:  $m \approx 0.035 \text{ kg/s}$ ; volume flow of coolant cycle:  $V = 2450 \text{ ml/s}$ .

**4.4 Calculation of compressor emissions**

Required compressor emissions:  $q_v = 136 \text{ ml/r}$ ;

the cooling volume of the compressors must be in accordance with the selected system; according to the performance curve of Dks117, the indicated efficiency of the compressor is:  $\eta_i = 0.82$ ; the actual power consumption of the machine is:  $N = 2.93 \text{ KW}$ . After calculation, the power actually consumed by the compression machine is deducted by the power output of the engine. With  $2.93/20 = 14.7\%$ , the power consumption ratio is therefore permissible according to the compressor power prescription table and can be matched [17].

**4.5 Calculation of condenser capacity**

Condensed heat exchange capacity:  $Q_{cool} = 5.26 \text{ KW}$ ; heat exchanger load ratio:  $Q: Q_{cold} = 1: 1.14$ .

To obtain accurately the weight of the heater in a small car. Many factors need to be taken into account, for example, local losses, which are divided into pressure and pipeline losses. Evaporator cooling volume  $Q_{vapor}$  and system cooling quantity  $Q_e$  should be consistent, so  $Q_e = Q_{vapor} = 4611.8 \text{ W}$ .

**4.6 Determination of ventilation capacity**

Input temperature  $t = 28^\circ\text{C}$ ; input relative humidity  $\Psi = 50\%$ ; input  $h = 58.5 \text{ KJ/kg}$ ;

output temperature  $T = 10^\circ\text{C}$ ; output relative moisture  $\Psi = 70\%$ ; output  $h = 23.5 \text{ KJ/kg}$ .

Ventilation wind capacity:  $v \approx 474 \text{ m}^3/\text{h}$  Wind capacity has a crucial role in the evaporator. Therefore, the transmission of wind volume requires strict control.

**V. RESULTS AND DISCUSSION**

This paper first uses Fluent software for numerical simulation and then *PDD* and *PMV* for determining the leaf to optimally accommodate body heat comfort. Then design parameters such as the car air-conditioning cooling cycle and the transmission of wind volume to meet the requirements of human thermal comfort.

The first step is to determine the optimum latitude of the leaf, and this paper uses Fluent for a numerical simulation, and the results are determined by *PDD* and *PMV*. First, use Fluent to compile the internal flow field in the car. Then add the theoretical formula to obtain the values of the different latitudes of the sheet. Finally, according to the theory formula of *PMV* and *PDD*, add the data obtained from the simulation, thereby making a judgment of human comfort compared to Table 2. Based on the numeric simulation results, we find that when the sheets are 30 degrees wide, because the latitude is smaller, the passengers in the rear seat feel the higher wind volume and the lower temperature. When the latitudes are 60 degrees, because of the larger latitude, the wind is less easily blown to the back seat, resulting in a lower wind and a higher temperature perceived by the back passenger.

The second step is the setting of the air conditioning cooling parameters. The following data can be obtained by calculating parameters such as air conditioning cooling quantity and delivering wind capacity to achieve optimal thermal comfort for the human body. First of all, the conditions in the vehicle are set, and then the heat balance relationship, cooling cycle relationship, and cooling circulation flow are determined. Finally, the data is brought into the calculation of the determination value of each parameter, and the optimum parameter is obtained by comparison.

This is the result of the calculation. Data can be obtained from the thermal balance ratio formula,  $Q_e=4521.4W$ . Among them,  $Q_1=867W$ ,  $Q_2=159W$ ,  $Q_3=189W$ ,  $Q_4=1604.3W$ ,  $Q_5=775.5W$ ,  $Q_6=96W$ , and  $Q_7=830.6W$ . According to the data analysis, the largest distribution of heat load is about 35% of windshield glass, followed by about 20% of the fence structure. Therefore, in order to reduce the heat load in the car, it should be based on improved body insulation and window glass material. With regard to the calculation of the cooling volume, the result is that when the speed of the vehicle reaches 40 km/h, the system cooling capacity should reach about 4611.8W. Taking into account the dirt from the outside as well as the local heat loss of the car. Therefore, the general heat exchanger load ratio on the car is 1: 1.5 to 1: 2, that is, the heat exchange capacity of the condenser is  $Q_{cold}=6.9$  to  $9.2$  KW. Evaporator cooling volume  $Q_{vapor}$  and system cooling quantity  $Q_e$  should be consistent;  $Q_e=Q_{vapor}=4611.8W$ . As for the determination of the ventilation volume, because the air volume is too large if it is designed, it will cause costs and also cause unnecessary noise. An increase in the soundproofing will also generate increased costs, so it is difficult to arrange the fan layout. Another extreme aspect is that the humidity of the floor in the car cannot be averaged. Nor can stability be maintained if the air volume is too small. After the calculation of the ratio, the optimum output volume in this paper should be  $474$  m<sup>3</sup>/h.

By the above calculations and parameters determined, this paper obtained the optimum width of leaf rolling is  $45^\circ$ , the best case of the transmission of wind volume should be  $474$  m<sup>3</sup>/h, when the speed of the car reaches this paper, the system cooling volume should reach about  $4611.8W$ , heat exchanger load ratio 1:1.5~1:2 about.

## VI. CONCLUSIONS

This design uses Gambit software to calculate the speed field and temperature field values in the air-conditioned vehicle cabin and uses Fluent flow field calculation software to numerically simulate and analyze the flow field in the cabin. On the basis of the predecessor, a calculation model was proposed to evaluate the heat comfort of the human body in the car room under an uneven thermal comfort environment. By analyzing the temperature cloud chart in the car, speed vector chart, flow chart, etc., and after processing the numerical calculation of the display flow field, a comparative analysis and evaluation of human thermal comfort in the chamber of various operations was carried out, and the data for the optimum thermal comfort of the human body was obtained. This is important for improving the structure and design of

the internal environment for the air conditioning system while using simulation software for data analysis to solve the high cost of the vehicle.

## ACKNOWLEDGEMENTS

This work described in this paper was supported by The Research Funding Of GDUPT, Research on Lagrangian Coherent Structure Analysis of Heat Sink For Heat Transfer Performance With Piezoelectric Fan, Special Project of Taishi Excellent Training Plan in 2024. Special Project of Science and Technology Innovation Strategy of Guangdong Provincial Department of Science and Technology in 2024, (Project No.: 2024A0505050022).

## REFERENCES

- [1] QuiShi Wang. (2022) . Research on Thermal Environment and Human Thermal Comfort of Commercial Vehicle Localized Air Conditioning System Based on Thermoelectric Coolin. Learned scholar (Degree Thesis, School of Automotive Engineering).
- [2] Ma Jingfu & Wei Jingfu & Yang Yizhen & Wang Chen & Dai Bofu. (2020) . Effects of local radiation temperature on thermal comfort based on a human thermal adjustment model. Zhejiang Polytechnic University Journal (Natural Science Edition) (01), 130-135.
- [3] JinCheng Xu. (2022) . Study on Thermal Comfort Evaluation and Optimization of an SUV Passenger Compartment Considering Heating Load. Master (degree thesis, Jilin University).
- [4] Wang BaoGuo & Jin Yanmei & Liu Shuyan. (2005) . Calculation Model and Numerical Simulation of Cabin Thermal Environment. Human Effectiveness (01), 1-4.
- [5] YangYang Guo. (2017) . Analysis on Indoor Thermal Comfort of a Tourist Bus based on CFD Abstract. (Master's Degree, Xiamen Institute of Technology).
- [6] SUN Zhan-peng & ZHU Hai-rong & CAO Ya-chao & LIU Qing-gang. (2019) . Curriculum Construction of the Course "Principle and Design of Heat Exchangers". Internal combustion engines and accessories (20), 280-281.
- [7] Zhang Wenge. (2012) . Optimal design of vehicle air condition Base on thermalcomfort of human body. Master (degree thesis, Hunan University).
- [8] SHI Lu. (2013) . Effect of Illumination and Color Temperature of Lighting on Human Thermoregulation. JOURNAL OF SHNGHAIJIAOTONG UNIVERSITY (10), 1616-1620.
- [9] Tong Mei & Chen Lili & Wang Bo & He Yuan & Yu Sisi. (2014). Human Body Temperature Adjust and Winter Cold-Resistant Clothing in Analysis. China Individual Protection Equipment (01), 13-15.
- [10] Yadollah Farzaneh & AliA. Tootoonchi. (2008) . Controlling automobile thermal comfort using optimized fuzzy controller[J]. Applied Thermal Engineering. (14).
- [11] Bárbara Torregrosa-Jaime & Filip Bjurling & José M. Corberán & Fausto Di Sciullo & Jorge Payá. 2014.

- Transient thermal model of a vehicle's cabin validated under variable ambient conditions[J]. Applied Thermal Engineering.
- [12] Yining Sun. (2012). Evaluation and Analysis of Thermal Comfort on Vehicle HVAC. Master (degree thesis, Jilin University).
- [13] ZHAO Bo-yuan & LI Jiang-fei & WANG Ya-fei & XIE Ding-mei.(2016).Calculation of Driven Square Cavity Flow Based on SIMPLE Method.辽宁化工(06), 760-763.
- [14] XU Jin-cheng. (2022) .Study on Thermal Comfort Evaluation and Optimization of an SUV Passenger Compartment Considering Heating Load .Master (degree thesis, Jilin University).
- [15] MA Feng-ge. (2023). Optimization of air supply mode of automobile air conditioning based on the thermal comfort of passenger cabin environment. Master (degree thesis, Industrial University of Inner Mongolia).
- [16] Wang Binbin. (2018) .Analysis and Optimization of Thermal Comfort on Localized Automotive Air Conditioning. Master (degree thesis, Jilin University).
- [17] GUO Fang-cheng. (2021) .Research on Calculation Method for Discharge Pressure of Refrigeration Compressor. Daily electrical appliances (08), 63-65+75.
- [18] Xijie Hu. (2023) .Analysis and Optimization of Aerodynamic Performance of Small Electric Car Body Based on FLUENT. (Master's Degree, Yangzhou University).

# Research on Noise Mode Prediction of Air Conditioner Based on Training Neural Network Method

Ruo-Yu Yang, Yan-Zuo Chang\*, Jin-Ping Chen, Jian-Ting Lai, Ren-Jia Qin

Energy and Power Engineering, Guangdong University of Petrochem Technology (GDUPT), Maoming525000, China

\*Corresponding author: m18899891470@163.com

Received: 15 Jul 2024,

Receive in revised form: 19 Aug 2024,

Accepted: 27 Aug 2024,

Available online: 31 Aug 2024

©2024 The Author(s). Published by AI  
Publication. This is an open-access article  
under the CC BY license

(<https://creativecommons.org/licenses/by/4.0/>).

**Keywords**— Air conditioning, Air-conditioning noise, neural networks

**Abstract**— This research establishes forecasting models for air-conditioning noise through training-type neural networks, which can improve the accuracy of the forecast, reduce costs and time, optimize system design and improvement, improve user experience and reduce environmental impact. This study uses Matlab to build training neural networks and uses the Levenberg-Marquardt. The results showed that the neural networks built by the training methods and the data and model combination were excellent. Therefore, the neural network to establish the model for the forecast of air conditioning noise has a significant effect for future air conditioner companies in the research and improvement of the noise.

## I. INTRODUCTION

Air-conditioning has become an indispensable part of modern society in recent years, with the continuous development of science and technology, and has been applied in almost all parts of the world. It not only provides people with a comfortable indoor environment, but also plays an important role in many areas, such as industrial production, health care, information technology and so on. But as people's quality of life improves, the demand for air conditioning increases, and air-conditioning noise becomes a problem that cannot be neglected [1]. Excessive air-conditioning noise can affect the quality of sleep, resulting in difficulties in getting to sleep, being awake or not sleeping well in the long term; in an office or study environment, persistent noise distracts attention and reduces work and learning efficiency, affecting work and academic performance; in a home environment, excessive noise of air conditioning can affect people's leisure and leisure experiences, making their living environment uninhabitable and reducing their quality of life; persistence of noise stimulus can lead to anxiety, stress and unrest, increasing the risk of mental health problems, especially for children and older people.

Excessive air-conditioning operating noise can have a multi-faceted impact on people's lives and work environments, including sleeping noise that can disrupt harmony between neighbours, provoke complaints and disputes, and affect interaction between the community environment and residents; and prolonged exposure to high noise environments can lead to hearing loss, cardiovascular disease and other health problems that have adverse effects on physical health. Users of air-conditioning want to reduce noise, noise as a very important R&D indicator of air conditioning, the developer will include noise reduction as one of the main considerations when developing the air conditioner. So this study hopes to be able to build a training neural network for the noise pattern of air conditioning through Matlab to conduct a training, so that a forecast of the noisy patterns of the air conditioner, and then in the beginning of the R & D design of air-conditioning, to fundamentally reduce the impact of noise on people.

The noise source of air conditioning is mainly due to two aspects, one is the noise generated by the air conditioner during normal operation, and the other is noise produced during the abnormal operation of the air-

conditioning [3]. For air conditioning abnormal noise problem treatment, we need to know the source of abnormal noise, judging whether high frequency noise or low-frequency sound, whether continuous or instantaneous sound, electromagnetic or resonance noise etc [4]. Air conditioning is a highly integrated product, in the R&D design of different models of air conditioning consisting mainly of compressors, fans, winds and outlets, pipes and accessories, control boards and circuit components. And the size of the noise is closely related to these air-conditioning components. So there are a lot of factors that cause the noise of the air conditioning [5]. The wind speed is also sometimes the reason why the noise is produced, which is due to the friction that occurs in the process of air flow, mainly from the wall of the pipe, vent and valve, and when the speed of the wind will become bigger, which leads to noise increases, so the size of noise at the time depends mainly on the amount of wind speed [6].

The issue of neural network validation was first raised in 2010 by Pulina and others, who used a neural input-based separation refinement method, and used the ideas and techniques of the formalization method for the first time in the safety assessment of the neural networks [14]. The development of neural networks dates back to the 1950s, but breakthroughs have only been made in recent years. The sensor is one of the earliest models of a neural network, proposed by Frank Rosenblatt in 1957. It is a simple one-layer neural network that can be used for binary classification problems [15]. The introduction of the sensor attracted widespread attention from the academic community and industry, but due to its limitations, if only solve the linear divisibility problem, resulted in later gradual elimination. After the study of sensors was eliminated, neural networks entered a hibernation period, due to the lack of effective training algorithms and computational resources, and the suspicion of neural network capabilities. In the late 1980s and early 1990s, the introduction of reverse transmission algorithms reignited the enthusiasm for neural network research [16]. This algorithm allows the Multi-Layer Perceptron (MLP) to be trained to overcome the limitations of the sensor. The results of this period include Backpropagation Through Time (BPTT) and Levenberg-Marquardt. During this period, Multi-Layer Perceptron (MLP) were widely used, especially in the fields of finance, medicine, and speech recognition. In addition, some important algorithms and models such as Support Vector Machines (SVM) and Gaussian Mixture Model (GMM) have been proposed and applied. With the continuous improvement of computing capabilities and the development of big data technology, deep learning has begun to emerge [17]. The introduction of Convolutional Neural Networks (CNN) promoted the

development of the field of computer vision, and the application of circular neural network such as Long Short-Term Memory (LSTM) contributed to the advancement of natural language processing.

## II. USING MATLAB TO BUILD A NEURAL NETWORK FORECAST MODEL

This study uses Matlab to build a neural network forecast model. first of all, processing the noise data, and then to the Levenberg- Marquardt, the Bayesian Regularization, and the Quantitative Conjugate Gradient were compared, and used by the Levenberg- Marquardt method trains air-conditioning noise data, discusses the results, losses, training performance and learning rate of the model, analyzes the matching effects of the data and the model and exports the results chart.

### 2.1 Noise data processing formula

The formula for noise calculation can vary depending on the source of noise and the specific situation. Here are some common noise calculation formulas and their application scenarios:

(1)Sound Pressure Level (SPL):

$$SPL = 20\log_{10}\left(\frac{p}{p_0}\right) \quad (1)$$

$p$  is the sound pressure, and  $p_0$  is the reference sound pressure (generally taken as the standard atmospheric pressure, approximately 20 micropascal).

(2)Sound Power Level (SWL):

$$SPL = 10\log_{10}\left(\frac{w}{w_0}\right) \quad (2)$$

$w$  is the sound power, and  $w_0$  is the reference sound power (generally taken as  $10^{12}$  watt).

(3)Total Sound Level:

The total sound level can be obtained by adding the sound pressure level of each sound source, with the formula as follows:

$$L_{total} = 10\log_{10}\left(\sum_{i=1}^n 10^{\frac{L_i}{10}}\right) \quad (3)$$

$L_i$  is the sound pressure level of the first  $i$  sound source, and  $n$  is the number of sound sources.

(4)Weighted Sound Level:

The calculation of air-conditioning noise usually involves factors such as acoustic parameters and the working state of the air conditioning system.

$$L = L_r + 10\log_{10}\left(\frac{Q}{Q_r}\right) + K \quad (4)$$

$L$  is the total sound level of air conditioning (units: decibels, dB);  $L_r$  is the reference sound level, usually for the basic noise level when the air conditioner is not

working (unities: decibel, dB); Q is the amount of cooling or heat generated by air conditioners under a specific operation condition (unity: power, usually in watts);  $Q_r$  is the quantity of reference cooled or heat produced, typically for the cooling quantity or heating generated under the condition of air-conditioning design (unit: energy, W); K is the specific adjustment coefficient of the climate system, taking into account the effects of the various factors of the air- conditioning system on the noise.

**2.2 Artificial Neural Network**

Artificial Neural Network (ANN) is a mathematical model for information processing based on the simulation of the neurosynthesis connected organs of the human brain [11]. A class neural network is a machine learning model inspired by the human nervous system. It consists of a large number of artificial neurons (also known as nodes or units) that transmit and process information through connections [31].

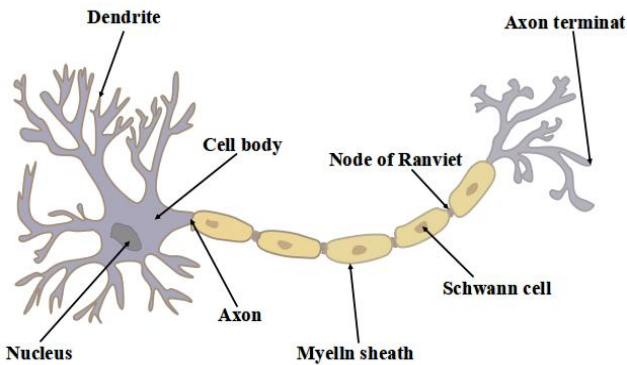


Fig. 1 Neural

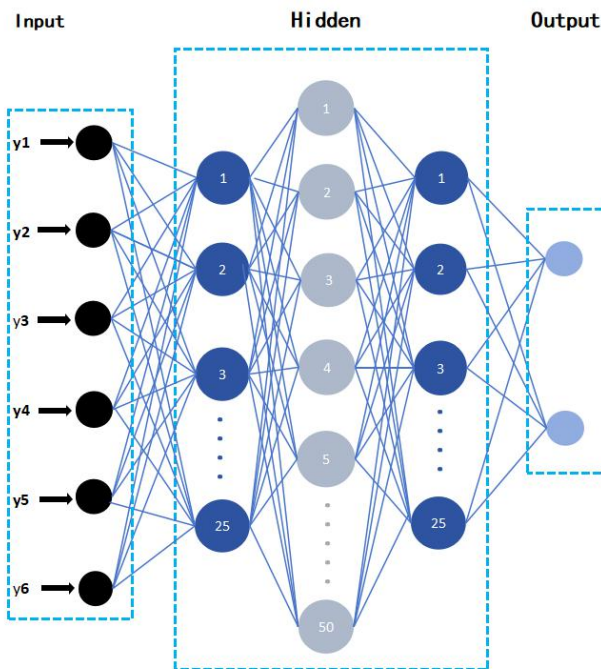


Fig. 2 Artificial Neural Network

In observing the results of neural network training, common evaluation indicators include Mean Squared Error (MSE) and Correlation Coefficient (R). These indicators can be used to assess the predictive performance and suitability of models.

(1)MSE:

$$MSE = \frac{1}{N} \sum_{i=1}^N (y_i - \hat{y}_i)^2 \tag{5}$$

n is the number of samples,  $y_i$  is the real value,  $\hat{y}_i$  is the predicted value.

The smaller the MSE, the better the model matches the data.

(2)R:

$$R = \frac{\sum_{i=1}^n (y_i - \bar{y})(\hat{y}_i - \bar{\hat{y}})}{\sqrt{\sum_{i=1}^n (y_i - \bar{y})^2 \sum_{i=1}^n (\hat{y}_i - \bar{\hat{y}})^2}} \tag{6}$$

$\bar{y}$  and  $\bar{\hat{y}}$  are the mean values of true values and predicted values, respectively.

R has a range of values ranging from -1 to 1, near 1 represents positive, near -1 is negative and near 0 is irrelevant.

**III. BUILD A MODEL WITH MATLAB**

Compare the regression performance of the three training methods: the Levenberg-Marquardt, the Bayesian Regularization, and the Quantitative Conjugate Gradient, the Levenberg- Marquardt, the Bayesian Regularization , and the Quantitative Conjugate Gradient, have Correlation Coefficient R of 0.99519, 0.99913 and 0.98809, respectively, so the Levenberg-Marquardt method predicts better. This study uses Matlab to apply the Levenberg-Marquardt method is used to build training neural networks.

**3.1 The Levenberg-Marquardt**

Levenberg-Marquardt (LM) is an optimized algorithm for training neural networks, commonly used for regression problems and multi-layer forward input networks. It is a gradient-based algorithy that combines the advantages of the Steepest Descent Method and Gauss Newton method, and is widely used in practice in training regression issues and multilayer neural network [32]. It can rapidly converge to local optimum solutions, and has faster convergence rates, better stability and robustness [19].

Here is the formula for the LM algorithm:

(1)Objective Function:

Objective Function is usually expressed as a loss function or cost function, used to measure the difference between the model's forecast value and the real label.

$$L(w) = \frac{1}{2N} \sum_{i=1}^N (y_i - f(x_i, w))^2 \tag{7}$$

N is the number of samples,  $y_i$  is the real label,  $f(x_i, w)$  is the predicted value of model for sample  $x_i$ , and  $w$  is the model parameter.

(2)Gradient Function:

Gradient Function represents the gradient of the target function with respect to the parameter, which is used to guide the direction of the updated parameter.

$$\nabla L = -\frac{1}{N} \sum_{i=1}^N (y_i - f(x_i, w)) \nabla f(x_i, w) \tag{8}$$

(3)LM Step:

The LM Step is the step length of the parameter update in Levenberg-Marquardt, which achieves rapid convergence and stability through Balanced Gradient Descent and Newton Method.

$$\Delta w = (J^T J + \lambda I)^{-1} J^T \delta \tag{9}$$

J is the jacobian matrix of the target function,  $\lambda$  is the adjustment parameter of the LM algorithm, and  $\delta$  is the gradient of the goal function.

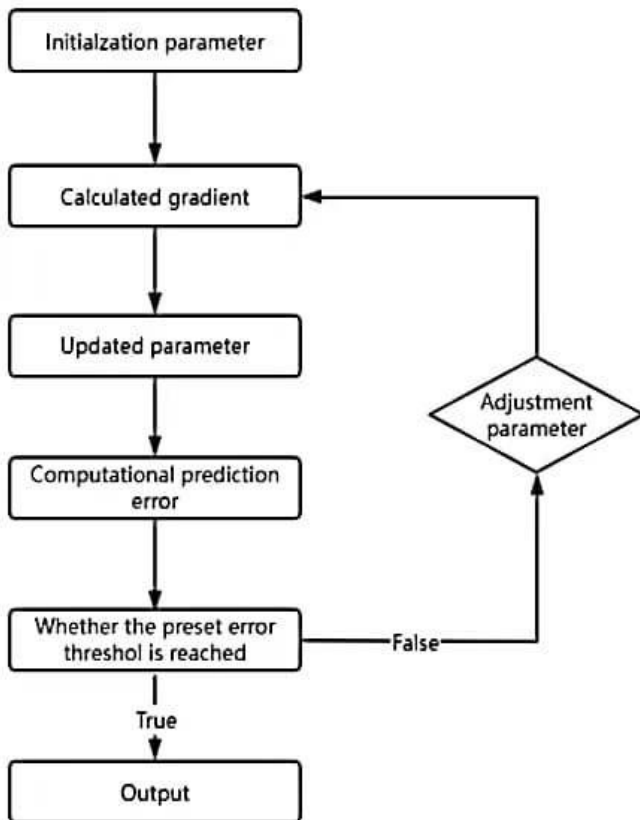


Fig.3 Flow chart of Levenberg-Marquardt

Combine raw data, and LM algorithm formula. LM training results are as shown in Figure 4, from which the LM method neural network model is comparatively good;

LM training losses are like Figure 5, the gradient of the training loss curve is 0.23222 which means that the loss function has decreased by an average of 0.23222 units in each iteration; the performance of LM mode Artificial Neural Networks is like Figure 6, which is gradually closer to optimum performance after the eighth round of training, and at the tenth round achieves the optimum validation performance, as shown by Figure 16, generally overlapping with the optimal performance value; the learning rate of the LM method is as shown on Figure 7, from which it is shown that the rate of learning of this Neural Network training model is 0.001; and the validation failure (LM validation Fail) as shown at Figure 8, means that verification failure occurred in the sixth training cycle.

Training result

Training start time: 2024-05-08 17:14:20  
Layer size 10

	Observed Values	MSE	R
train	56	0.1178	0.9970
Verification	12	0.1708	0.9972
Tests	12	0.5681	0.9760

Fig.4 LM training results

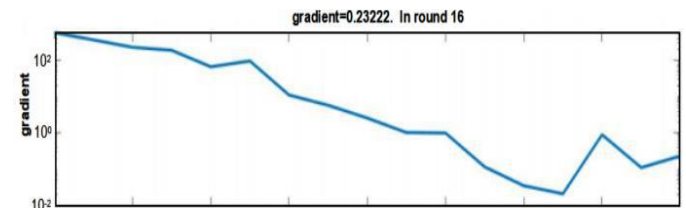


Fig.5 LM training losses

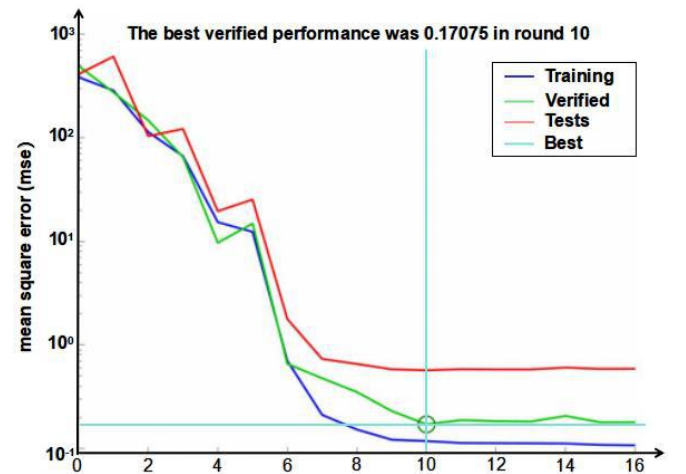


Fig.6 The performance of LM mode Artificial Neural Networks

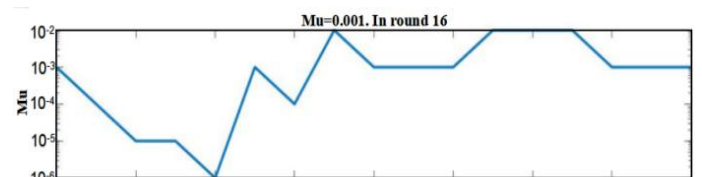


Fig.7 The learning rate of the LM method

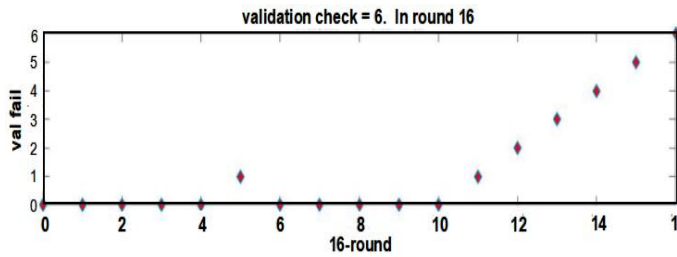


Fig.8 LM validation Fail broken line graph

#### IV. ARTIFICIAL NEURAL NETWORK TRAINING RESULTS

as shown in Figure 9; verification regression related coefficient is 0.99717, as shown on Figure 10; test regression related coefficient is 0.97599, as shown at Figure 11; total regression related coefficient is 0.99519, as seen in Fig.12.

Neural network training regression diagrams are commonly used to show the relationship between the predicted results of a model and the actual target value to help users evaluate the performance of the model in the regression task. By observing the neural network training regression diagram, users can intuitively understand the performance of the model in the regression task, including the accuracy of the prediction, the degree of deviation and the adjustment effect. This helps to assess the performance of the model, identify problems with the model and guide further model adjustment and improvement. It is not difficult to see through the following regression diagram that the predicted value of the neural network training model based on the LM method and the linear correlation between the actual observation values is very high, close to 1, indicating that the model has a high degree of adaptation on the training data, the prediction and optimization of air conditioning noise has a good effect.

Thus, the R value of 0.99519 represents a high level of linear correlation between the model's predicted value and the actual observed value, indicating that the model has a very good matching effect in the regression task. This means that the model is very similar to the trend between the predicted value and the actual value, can accurately capture the change in the target variable, and has a high predictive ability.

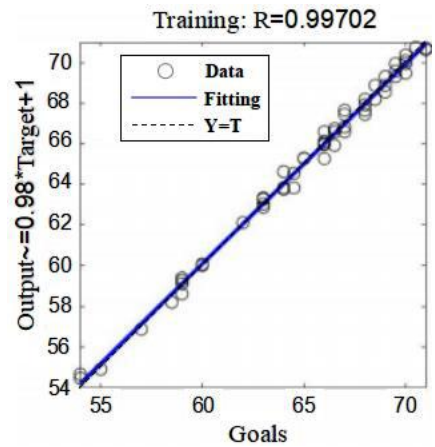


Fig.9 Training regression graph

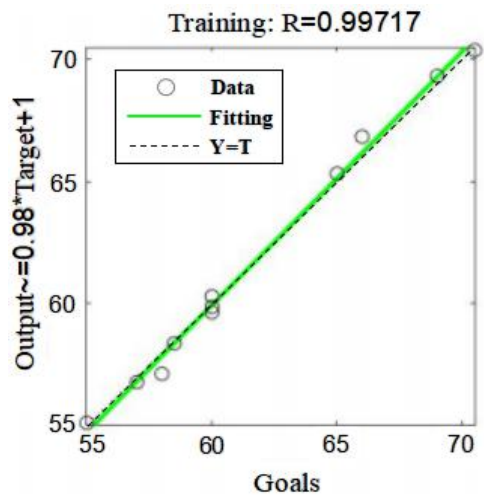


Fig.10 Verification regression graph

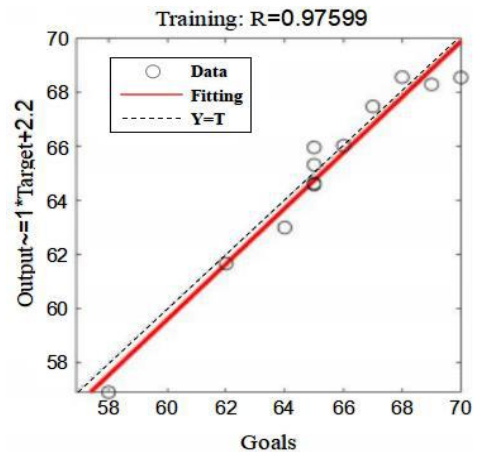


Fig.11 Test regression graph

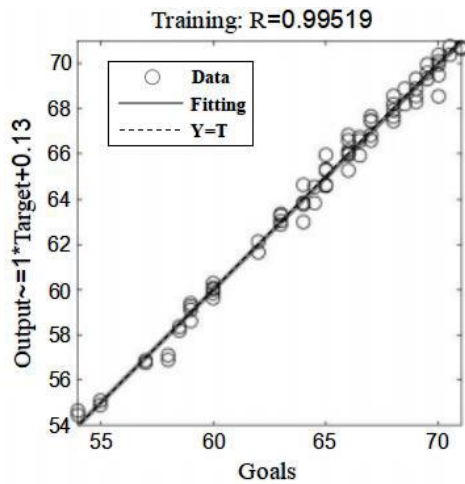


Fig.12 Regression graph

## V. CONCLUSION

The conclusion of the Levenberg-Marquardt method training on neural networks is that the model works well on the training data, and there is a high linear correlation between the predicted value and the actual observed value. It should be noted, however, that these conclusions are based solely on the performance of the training data and that generalization performance also requires further evaluation in the validation set or test set to ensure that the model performs well on unprecedented data.

It should also be noted that after the completion of Artificial Neural Network training, a comprehensive evaluation and validation of the model is required and the model and training strategy is adjusted according to the evaluation results to ensure that the model achieves the desired effect in practical applications. You can reasonably design the air conditioning system wind path, selecting the appropriate installation position to reduce the effect of static pressure on the air-conditioning noise. On the one hand, increasing the wind volume can increase the efficiency of air flow and improve the performance of the air-conditioning system; on the other hand, measures such as optimizing the wind path design, using noise-reducing materials, choosing a low-noise fan, etc., are needed to reduce the impact of wind volume on noise.

## ACKNOWLEDGEMENTS

This work described in this paper was supported by The Research Funding of GDUPT, Research on Lagrangian Coherent Structure Analysis of Heat Sink for Heat Transfer Performance with Piezoelectric Fan, Special Project of Taishi Excellent Training Plan in 2024. Special Project of Science and Technology Innovation Strategy of

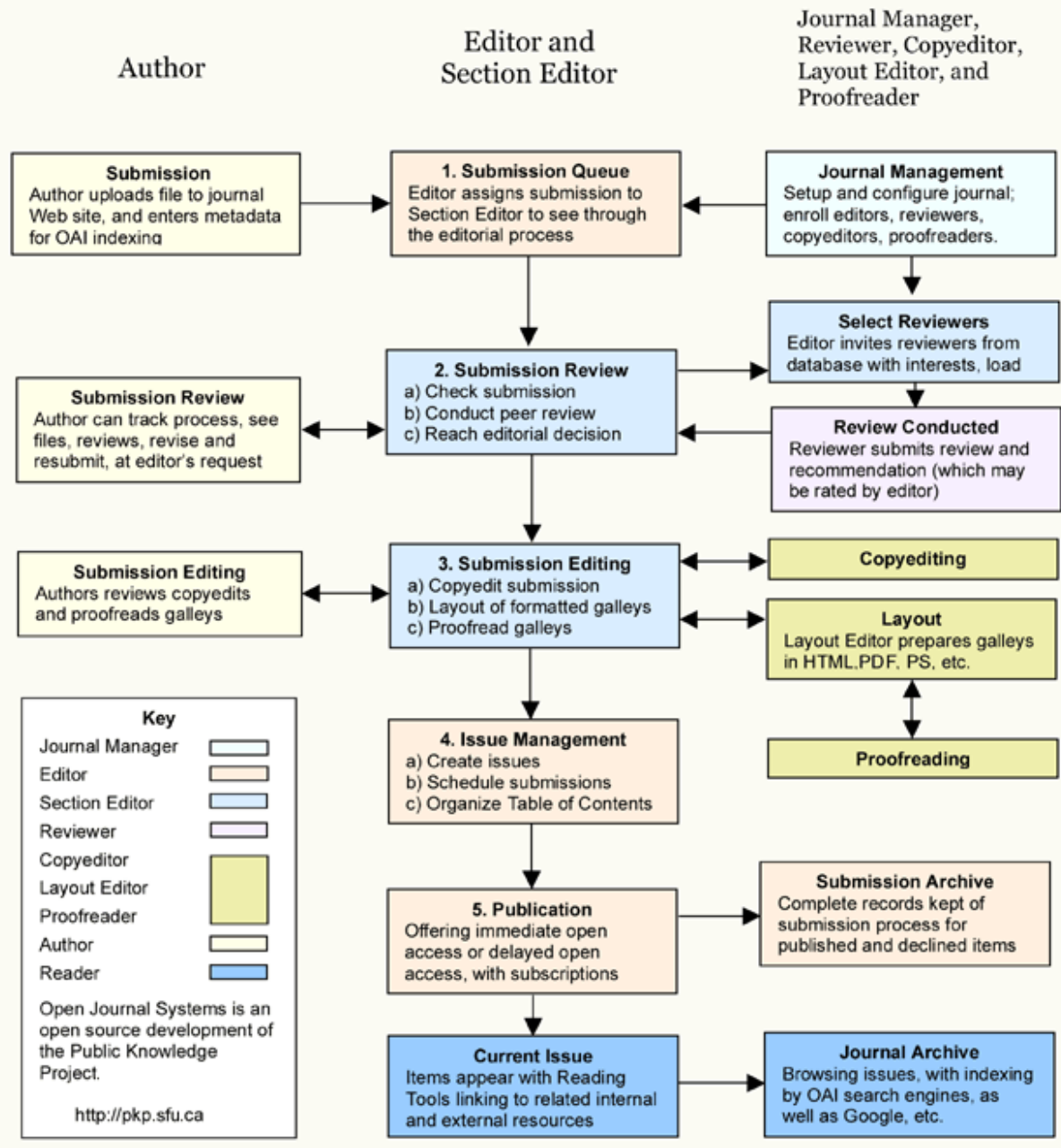
Guangdong Provincial Department of Science and Technology in 2024, (Project No.: 2024A0505050022).

## REFERENCES

- [1] Lu Zhiyun. (2014). Studies on sources, diagnosis and noise reduction of air-conditioning noise. *Scientific and technological perspectives* (13), 103.
- [2] Qiu Song. (2015). Noise analysis and control methods of air-conditioning indoor machines. *Technological innovation and applications*, (20), 152.
- [3] Zhou Yuan Huang. (2014). Experimental methods of control of air-conditioning noise. *Science and Technology*, (19), 101+203.
- [4] Chen Tian Zheng. (2021). Home appliances central air conditioning operation noise problem light analysis. *Cooling*, 40 (03), 45-49.
- [5] Liu Pyeong-woo & Huang-wi-chao. (2017). Comfort assessment of air-conditioning noise. *Science and Technology Horizons* (06), 323.
- [6] Chen Zhi Bing. (2020). Engineering noise control technology for the air-conditioning system of the Nantong Theatre. *Construction materials and decoration*, (03), 221-222.
- [7] Chen Wing, & Wang Dang. (2016). Research on new methods to reduce air-conditioning noise. *Science and Technology Vision*, (14), 154.
- [8] Liu Ming & Liu Liu. (2011). Analysis of improved indoor air-conditioning noise exploration. *Home appliances technology*, (07), 62-63.
- [9] Churchill. (2019). Central Air Conditioning Noise Sources and Noise Reduction Initiatives. *Electronic World*, (15), 192-193.
- [10] Liu Yuan & Zhao Huangmin. (2017). An experimental study to improve air-transmitting noise in the air-conditioning system. *Daily electrical appliances*, (07), 55-57.
- [11] Liu Zhao, Liang Kai-won, Dong-kin-ring. (2024). Construction of a financial early warning model for listed companies based on artificial neural networks. *Operations and management*, (03), 69-77.
- [12] Chen Zhi Li, Liang Shui, Li Khao Ho, etc. (2023). A comparative study of DLC synthesis performance predictions based on different neural networks. *Vacuum Science and Technology Journal*, 43 (08), 665-673.
- [13] Mariah Carey. (2024). Neural Networks Application Analysis in Crop Water Demand Estimates. *Intelligent Agriculture Guide*, 4 (09), 9-12.
- [14] Liu Sheng Xin, Yang Pong Fei, Zhang Liu, etc. (2024). Complete Neural Network Authentication Acceleration Technical Overview. *Software Paper*, 1-31.
- [15] Pennington Conan. (2020). Low-pressure circuit breaker health monitoring and failure diagnostics research (master's thesis, Hubei Industrial University).
- [16] Cao Cao Lin. (2019). Deep learning based wireless network traffic prediction (master's thesis, Xi'an University of Electronics and Technology).
- [17] Shri Qian & Sun Huang. (2009). Speaker-identified study based on the SMM-GMM hybrid model. *Helioguan Engineering Institute Journal (Natural Sciences Edition)*

- (04), 54-57.
- [18] Hong Xiaodong, Dong Huang, Lin Meeking, etc. (2023). Graphic neural networks predict the thermodynamic properties of molybdenum. *Journal of Chemical Engineering*, 74 (11), 4466-4474.
- [19] The Holy Army. (2024). Parallel electrophysical analysis based on Levenberg-Marquardt reactions. *Technical Journal of the Jiangsu Institute of Architecture*, 24 (1), 15-20.
- [20] Huang Pei, Lin Seong, Shen Tian Tao, etc. (2023). Based on the Bayesian normalized LSTM model, the per capita GDP forecast results – for example, in Fujian Province. *Economic and Trade Times*, 20 (6), 140-144.
- [21] Guo Haishim, Zhou Shi, Liu Pei, etc. (2024). Progress in the application of artificial neural networks in the field of mass spectrum. *Artificial Intelligence*, 1-10.
- [22] Chur, Yuan Yuan, Umbrella Ice. (2024). Based on improved experience of molecular decomposition with BiLSTM neural networks, low-end house atherosclerosis timescale forecast. *Journal of the University of Hunan (Natural Sciences Edition)*, 1-12.
- [23] Liu, J., Wen, X., & Jian, S. (2024). Toward better equity: Analyzing travel patterns through a neural network approach in mobility-as-a-service. *Transport Policy*, 153, 110-126.
- [24] A.V. F., O.K. S., & V.P.G. (2024). Multigroup Classification of Firing Pin Impressions with the Use of a Fully Connected Neural Network. *Programming and Computer Software*, 50 (1), 73-84.
- [25] Zhang, D., Lv, H., Yan, S., et al. (2024). Multi-objective neural network modeling and applications to microwave power amplifiers. *Microelectronics Journal*, 149, 106244.
- [26] Double, & High Tree Shine. (2024). Research on design and application of heating and air-conditioning energy-saving systems. *Technological innovation and applications*, 14 (13), 132-135.
- [27] Shao Meeling, & Wang Chenglong. (2023). *Shandong Industrial Technology*, (01), 100-103.
- [28] Liu Xiaoping, Du Qingdao, Zhang Into the East. (2015). Paper-oriented identification method based on BP neural networks. *Computer Applications and Software*, 32 (11), 176-179.
- [29] Nguyen. (2023). The study of the technique of selection of the external quality of tomatoes based on the enveloping neural networks. *Xinjiang Agricultural University*.
- [30] Hshu Hui, Li Zhi Jing, Li Yuan, etc. (2023). Remote sensing image classification based on cost-sensitive convoluted neural networks. *Computer applications and software*, 40 (05), 253-261.
- [31] Yellow Valley. (2020). Identity certification studies based on step information (master's thesis, University of Electronics and Technology).

# OJS Editorial and Publishing Process



~JAERS Workflow~

## Important links:

### Paper Submission Link:

<https://ijaers.com/submit-paper/>

### Editorial Team:

<https://ijaers.com/editorial-board/>

### Peer Review Process:

<https://ijaers.com/peer-review-process/>

### Publication Ethics:

<https://ijaers.com/publication-ethics-and-publication-malpractice-statement/>

### Author Guidelines:

<https://ijaers.com/instruction-to-author/>

### Reviewer Guidelines:

<https://ijaers.com/review-guidelines/>

---

## Journal Indexed and Abstracted in:

- Qualis-CAPES (A2)-Brazil
- Normatiza (Under Review- Ref.020191511)
- NAAS Score: 3.18
- Bielefeld Academic Search Engine(BASE)
- Aalborg University Library (Denmark)
- WorldCat: The World's Largest Library Catalog
- Semantic Scholar
- J-Gate
- Open J-Gate
- CORE-The world's largest collection of open access research papers
- JURN
- Microsoft Academic Search
- Google Scholar
- Kopernio - powered by Web of Science
- Pol-Index
- PBN(Polish Scholarly Bibliography) Nauka Polaska
- Scilit, MDPI AG (Basel, Switzerland)
- Tyndale University College & Seminary
- Indiana Library WorldCat
- CrossRef DOI-10.22161/ijaers
- Neliti - Indonesia's Research Repository
- Journal TOC
- WIKI-CFP
- Scinapse- Academic Search Engine
- Mendeley-Reference Management Software & Researcher Network
- Dimensions.ai: Re-imagining discovery and access to research
- Index Copernicus Value(ICV): 81.49
- Citeseerx
- Massachusetts Institute of Technology (USA)
- Simpson University (USA)
- University of Louisville (USA)
- Biola University (USA)
- IE Library (Spain)
- Mount Saint Vincent University Library ( Halifax, Nova Scotia Canada)
- University Of Arizona (USA)
- INDIANA UNIVERSITY-PURDUE UNIVERSITY INDIANAPOLIS (USA)
- Roderic Bowen Library and Archives (United Kingdom)
- University Library of Skövde (Sweden)
- Indiana University East (campuslibrary (USA))
- Tilburg University (The Netherlands)
- Williams College (USA)
- University of Connecticut (USA)
- Brandeis University (USA)
- Tufts University (USA)
- Boston University (USA)
- McGill University (Canada)
- Northeastern University (USA)
- BibSonomy-The blue social bookmark and publication sharing system
- Slide Share
- Academia
- Archive
- Scribd
- ISRJIF
- Cite Factor
- SJIF-InnoSpace
- ISSUU
- Research Bib
- infobaseindex
- I2OR
- DRJI journal-repository



### AI Publication

International Journal of Advanced Engineering Research and Science (IJAERS)

104/108, Sector-10, Pratap Nagar, Jaipur, India